



Imaging through random discrete-scatterer dispersive media

Elizabeth Bleszynski
MONOPOLE RESEARCH THOUSAND OAKS CA

08/27/2015
Final Report

DISTRIBUTION A: Distribution approved for public release.

Air Force Research Laboratory
AF Office Of Scientific Research (AFOSR)/ RTB
Arlington, Virginia 22203
Air Force Materiel Command

REPORT DOCUMENTATION PAGE			Form Approved OMB NO. 0704-0188	
Public Reporting burden for this collection of information is estimated to average 1 hour per response, including the time for reviewing instructions, searching existing data sources, gathering and maintaining the data needed, and completing and reviewing the collection of information. Send comment regarding this burden estimates or any other aspect of this collection of information, including suggestions for reducing this burden, to Washington Headquarters Services, Directorate for Information Operations and Reports, 1215 Jefferson Davis Highway, Suite 1204, Arlington, VA 22202-4302, and to the Office of Management and Budget, Paperwork Reduction Project (0704-0188,) Washington, DC 20503.				
1. AGENCY USE ONLY (Leave Blank)		2. REPORT DATE 20 August 2015		3. REPORT TYPE AND DATES COVERED Final report 15 April 2012 – 14 April 2015
4. TITLE AND SUBTITLE Imaging Through Random Discrete-Scatterer Dispersive Media			5. FUNDING NUMBERS Contract No: FA9550-12-1-0121	
6. AUTHOR(S) Elizabeth H. Bleszynski, Marek Ch. Bleszynski and Thomas Jaroszewicz				
7. PERFORMING ORGANIZATION NAME(S) AND ADDRESS(ES) Monopole Research 739 Calle Sequoia Thousand Oaks, CA 91360			8. PERFORMING ORGANIZATION REPORT NUMBER MON-10-15	
9. SPONSORING / MONITORING AGENCY NAME(S) AND ADDRESS(ES) Air Force Office of Scientific Research 875 N. Randolph Street, RM 3112 Arlington, VA 22203			10. SPONSORING / MONITORING AGENCY REPORT NUMBER not known	
11. SUPPLEMENTARY NOTES The views, opinions and/or findings contained in this report are those of the author(s) and should not be construed as an official Department of the Air Force position, policy or decision, unless so designated by other documentation.				
12 a. DISTRIBUTION / AVAILABILITY STATEMENT Approved for public release, distribution is unlimited.			12 b. DISTRIBUTION CODE	
13. ABSTRACT (Maximum 200 words) The objective of the effort was to develop a methodology which would allow enhanced signal transmission, high resolution range imaging and/or target detection through optically obscuring, dilute, discrete-scatterer media such as clouds, fog, dust and other aerosols. (A) Properties of chirped-train waveforms such as their multi-band power spectra and the resulting point spread and ambiguity functions were analyzed. Advantages of the utilization of chirped trains in "multi-spectral" imaging (i.e., imaging based on frequency sub-bands of the chirped train signal) allowing extraction of frequency dependent information with improved signal-to-noise ratio was observed. (B) Propagation of short infrared/optical pulses in dilute random media consisting of large, compared to the wavelength, scatterers was analyzed. A rigorous approach based on analytic complex-contour integration of numerically determined cut and pole singularities of the radiative transport equation solution in the Fourier space was developed. It was found that the intensity of a propagating pulse, in addition to the coherent ("ballistic") contribution and a long late-time diffusive tail, also exhibits a sharply rising early-time component that (i) can be attributed to the small-angle diffractive part of the scattering cross-section on medium particles, (ii) is attenuated proportionally to the nondiffractive rather than total cross-section, and (iii) can be extracted by high-pass filtering of the received pulse.				
14. SUBJECT TERMS discrete-scatterer media, random media, dilute media, radiative transport, dispersive media, early-time diffusion, frequency filtering			15. NUMBER OF PAGES SF298+32	
17. SECURITY CLASSIFICATION OR REPORT UNCLASSIFIED			16. PRICE CODE not known	
18. SECURITY CLASSIFICATION ON THIS PAGE UNCLASSIFIED		19. SECURITY CLASSIFICATION OF ABSTRACT UNCLASSIFIED		20. LIMITATION OF ABSTRACT UNCLASSIFIED

NSN 7540-01-280-5500

Std. 239-18

Standard Form 298 (Rev.2-89)
Prescribed by ANSI
298-102

GENERAL INSTRUCTIONS FOR COMPLETING SF 298

The Report Documentation Page (RDP) is used for announcing and cataloging reports. It is important that this information be consistent with the rest of the report, particularly the cover and title page. Instructions for filling in each block of the form follow. It is important to ***stay within the lines*** to meet ***optical scanning requirements***.

Block 1. Agency Use Only (Leave blank)

Block 2. Report Date. Full publication date including day, month, and year, if available (e.g. 1 Jan 88). Must cite at least year.

Block 3. Type of Report and Dates Covered.

State whether report is interim, final, etc. If applicable enter inclusive report dates (e.g. 10 Jun 87 - 30 Jun 88).

Block 4. Title and Subtitle. A title is taken from the part of the report that provides the most meaningful and complete information. When a report is prepared in more than one volume, repeat the primary title, and volume number, and include subtitle for the specific volume. On classified documents enter the title classification in parentheses.

Block 5. Funding Numbers. To include contract and grant numbers; may include program element number(s) project number(s), task number(s), and work unit number(s). Use the following labels:

C - Contract	PR - Project
G - Grant	TA - Task
PE - Program Element	WU - Work Unit Accession No.

Block 6. Author(s). Name(s) of person(s) responsible for writing the report, performing the research, or credited with the content of the report. If editor or compiler, this should follow the name(s).

Block 7. Performing Organization Name(s) and Address(es). Self-explanatory.

Block 8. Performing Organization Report Number. Enter the unique alphanumeric report number(s) assigned by the organization performing the report.

Block 9. Sponsoring/Monitoring Agency Name(s) and Address(es). Self-explanatory.

Block 10. Sponsoring/Monitoring Agency Report Number. (if known)

Block 11. Supplementary Notes. Enter information not included elsewhere such as; prepared in cooperation with....; Trans. of...; To be published in.... When a report is revised, include a statement whether the new report supersedes or supplements the older report.

Block 12a. Distribution/Availability Statement.

Denotes public availability or limitations. Cite any availability to the public. Enter additional limitations or special markings in all capitals (e.g. NORFORN, REL, ITAR).

DOD - See DoDD 4230.25, "Distribution Statements on Technical Documents."
DOE - See authorities.
NASA - See Handbook NHB 2200.2.
NTIS - Leave blank.

Block 12b. Distribution Code.

DOD - Leave Blank
DOE - Enter DOE distribution categories from the Standard Distribution for unclassified Scientific and Technical Reports
NASA - Leave Blank.
NTIS - Leave Blank.

Block 13. Abstract. Include a brief (*Maximum 200 words*) factual summary of the most significant information contained in the report.

Block 14. Subject Terms. Keywords or phrases identifying major subject in the report.

Block 15. Number of Pages. Enter the total number of pages.

Block 16. Price Code. Enter appropriate price code (NTIS *only*).

Block 17. - 19. Security Classifications. Self-explanatory. Enter U.S. Security Regulations (i.e., UNCLASSIFIED). If form contains classified information, stamp classification on the top and bottom of the page.

Block 20. Limitation of Abstract. This block must be completed to assign a limitation to the abstract. Enter either UL (Unlimited) or SAR (same as report). An entry in this block is necessary if the abstract is to be limited. If blank, the abstract is assumed to be unlimited.

REPORT DOCUMENTATION PAGE (SF298)
(Continuation Sheet)

MASTER COPY: PLEASE KEEP THIS "MEMORANDUM OF TRANSMITTAL" BLANK FOR REPRODUCTION PURPOSES. WHEN REPORTS ARE GENERATED UNDER THE ARO SPONSORSHIP, FORWARD A COMPLETED COPY OF THIS FORM WITH EACH REPORT SHIPMENT TO THE ARO. THIS WILL ASSURE PROPER IDENTIFICATION. NOT TO BE USED FOR INTERIM PROGRESS REPORTS; SEE PAGE 2 FOR INTERIM PROGRESS REPORT INSTRUCTIONS.

MEMORANDUM OF TRANSMITTAL

U.S. Army Research Office
ATTN: AMSRL-RO-BI (TR)
P.O. Box 12211
Research Triangle Park, NC 27709-2211

Reprint (Orig + 2 copies)

Technical Report (Orig + 2 copies)

Manuscript (1 copy)

Final Progress Report (Orig + 2 copies)

Related Materials, Abstracts, Theses (1 copy)

CONTRACT/GRANT NUMBER:

REPORT TITLE:

is forwarded for your information.

SUBMITTED FOR PUBLICATION TO (applicable only if report is manuscript):

Sincerely,

Contents

1 Objectives	2
2 Summary of the results	2
2.1 Imaging with multiple frequency bands using chirped train signals for the purpose of extracting information on frequency dependence of the scattering process	2
2.2 Imaging and communication with optical or infrared pulsed signals through obscuring random media	2
2.3 Doppler effects in time-resolved intensity of optical pulses propagating through moving particulate atmospheric media	5
3 Publications resulting from Grant # FA9550-12-1-0121	6
References	7
Appendices	8

1 Objectives

The objective of this effort was to develop a methodology which would allow enhanced signal transmission, high resolution range imaging and/or target detection through optically obscuring, discrete-scatterer media such as atmospheric clouds, fog, dust and other aerosols is of significant interest in defense as well as commercial applications.

2 Summary of the results

We briefly summarize here the areas of our work and the main results.

2.1 Imaging with multiple frequency bands using chirped train signals for the purpose of extracting information on frequency dependence of the scattering process

This development is based on a further exploration of the properties of chirped trains of wide-band pulses, described in Refs. [1, 2] Such signals possess a rich spectrum consisting of a sequence of frequency bands centered at multiples of the “fundamental frequency” defined by the average pulse-pulse time spacing. While we have previously considered only the lowest frequency band (the “first harmonic”) of the signal spectrum, the present work exploits also higher harmonics. Our theoretical and numerical analysis shows that, with the appropriate choice of the parameters of the pulses and the train, it is possible to form signals characterized by a number of separate frequency bands separated by gaps whose widths can be controlled by the parameters. We analyze properties of the point-spread functions resulting from application of such signals to imaging. The proposed approach allows forming multiple images based on frequency sub-bands, for the purpose of extracting information on the frequency dependence of the scattering processes.

The approach is described in detail in the paper entitled “Imaging with multiple frequency bands using chirped train signals“. The paper was submitted for publication to IEEE Transactions on Geoscience and Remote Sensing, and is attached to this report as Appendix A.

2.2 Imaging and communication with optical or infrared pulsed signals through obscuring random media

Imaging and communication with optical or infrared pulsed signals through obscuring random media (e.g., atmospheric clouds, fog, dust, or aerosols) is a long-standing and challenging problem, both experimentally and theoretically. From the experimental and applications perspective, a coherently detected pulse field preserves its time profile, but is strongly attenuated, at the rate proportional to the total cross-section of

the wave on an individual medium scatterer. The incoherently detected field intensity (or, more generally, the mutual coherence function (MCF)), although attenuated at a lower rate (proportional to the absorption cross-section) than the coherent field, develops a long diffusive tail which causes loss of resolution in imaging and loss of bandwidth in communication.

The principal goal of our project was to develop formulation for pulse forming, detection, and processing methods which would enhance the signal penetration through obscuring media, without compromising the range resolution in imaging or the bit rate in communication. The main idea was to utilize incoherently detected pulses (through measurements of their *intensity*), hence to take advantage of their reduced attenuation and, at the same time, to reduce the detrimental effects of diffusion by means of processing of the received signal.

We developed rigorous approach based on analytic complex-contour integration of numerically determined cut and pole singularities of the radiative transport equation solution in the Fourier space. In the context of simulations based on the developed algorithm, we found that the intensity of an optical pulse, propagating in a dilute random medium composed of scatterers large compared to the pulse carrier wavelength (a condition well-met in the atmospheric cloud propagation scenario), in addition to the coherent (“ballistic”) contribution and a long late-time diffusive tail, also exhibits a *narrow, sharply rising early-time diffusive component* which

- can be attributed to the small-angle diffractive part of the scattering cross-section on individual medium particles,
- is attenuated proportionally to the non-diffractive rather than total cross-section,
- can be extracted (due to its sharp rise and therefore rich high frequency content) by high-pass filtering of the received pulse, i.e., without the necessity of performing any of the time-gating procedures,
- is practically insensitive to the motion of medium constituents.

In Fig. 1 we show the time-resolved intensity distribution for two propagation distances $R_1 = 12 \ell_t$ and $R_2 = 16 \ell_t$ in the atmospheric cloud medium. The medium is characterized by the average water droplet size of $a = 5 \mu\text{m}$ and the scatterer number density of $n_0 = 10^9 \text{ m}^{-3}$, resulting in the coherent attenuation length of $\ell_t = 1/(n_0 \sigma_t) \approx 6 \text{ m}$. A coherent source emitting a Gaussian-modulated field of carrier frequency c/λ_0 , with $\lambda_0 = 0.633 \mu\text{m}$, resulting in intensity $S(t) = \exp(-t^2/2T_p^2)/(\sqrt{2\pi} T_p)$, with $T_p = 60 \text{ ps}$ was assumed. The time-dependent intensity clearly exhibits a distinctive early-time diffusion behavior, characterized by a narrow spike followed by a much broader late-diffusion maximum and a long diffusive tail. As the propagation distance increases, the broad diffusion shoulder starts overlapping the trailing edge of the early-time diffusion peak, but its sharply rising leading edge remains.

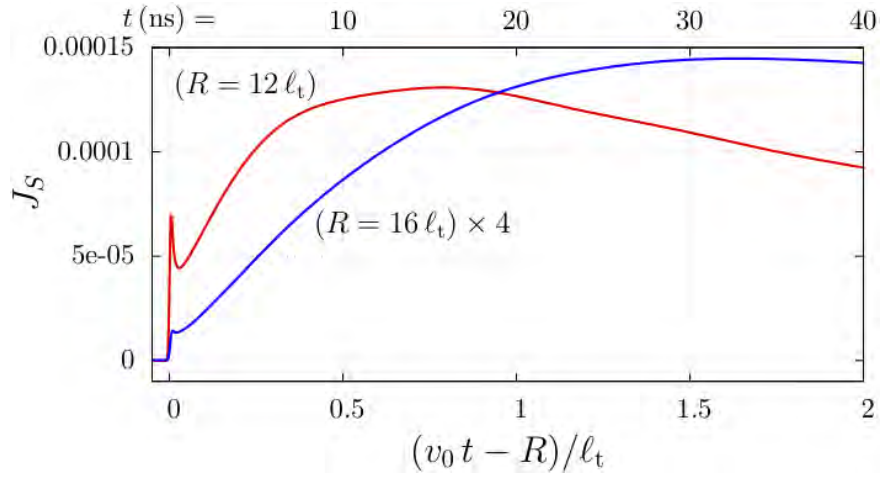


Figure 1: Intensity distributions showing early- and late-time diffusion behavior, for propagation distances $R_1 = 12 \ell_t$ and $R_2 = 16 \ell_t$, with the time scale indicated on top. The curves are visually indistinguishable from the Monte Carlo simulation results.

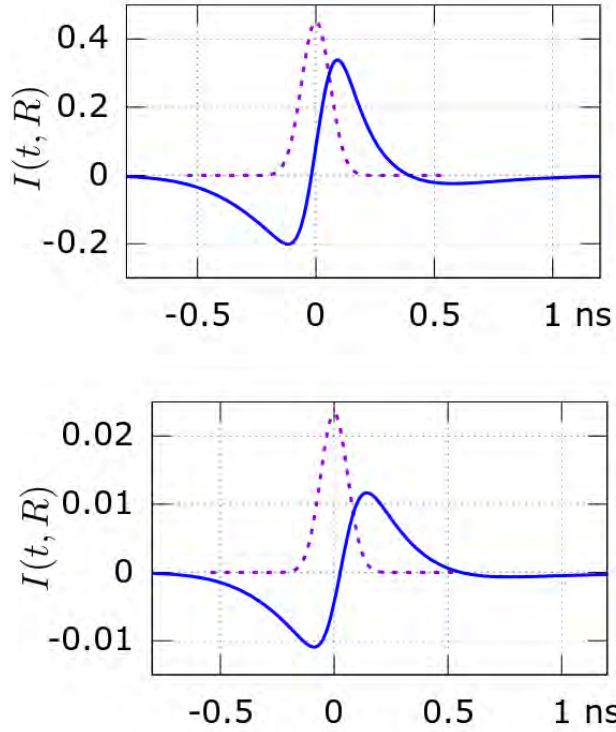


Figure 2: Filtered intensities for $R_1 = 12 \ell_t$ (top) and $R_2 = 16 \ell_t$ (bottom). Coherent contributions, *multiplied by factors 10^2 and 5×10^2* , are shown for reference.

Because of its sharp rise and therefore rich high-frequency content, the early-time diffusion can be extracted by a frequency gating procedure (i.e., without the necessity of applying any time gating). The filtered pulses are plotted in Fig. 2, for the same propagation distances, $R_1 = 12 \ell_t$ and $R_2 = 16 \ell_t$, as in Fig. 1. The coherent(“ballistic”) signal intensities corresponding to the same propagation distances are also included. (Please note the different scaling factors.) The plots show that the filtered early diffusive signals exceed those of the coherent intensity by the factor $\sim 100 - 500$.

To summarize, the developed approach allows to access part of the energy residing in the diffusive component of the intensity without compromising the resolution. This result may have important implications in high-resolution range imaging as well as communication through obscuring (atmospheric clouds, fog, dust, or aerosols) media.

The detailed description of the approach as well as some representative numerical results are presented in [3] and [4].

2.3 Doppler effects in time-resolved intensity of optical pulses propagating through moving particulate atmospheric media

We initiated the analysis of propagation of optical and infrared pulses through *moving* atmospheric particulate media. We generalized the radiative transfer equation to describe effects of the Doppler frequency shift on the time-resolved specific intensity of pulses. The overall effect of the frequency shift was estimated and found to be small, as a result of cancellation of phase variations in the the pulse intensity. In particular, that cancellation is nearly perfect in the pulse component associated with “early-time diffusion”, i.e., in the early-time steeply rising structure due to small-angle diffractive scattering on medium constituents.

The description of the approach and the preliminary results are presented in Appendix B. The paper is in preparation.

3 Publications resulting from Grant # FA9550-12-1-0121

E.H. Bleszynski, M.K. Bleszynski, and T. Jaroszewicz, “Amplification of signal intensity in imaging through discrete random media through signal interference gating and the use of mutual coherence function,” in *Ultra-Wideband Short Pulse Electromagnetics 10*, Springer 2014, pp. 89–99.

E. Bleszynski, M.K. Bleszynski, and T. Jaroszewicz, “Early-time diffusion in pulse propagation through dilute random media,” in *Optics Letters*, vol. 39, no. 20, pp. 5862–5865, 2014.

E. Bleszynski, M.K. Bleszynski, T. Jaroszewicz, and R. Albanese, “Imaging with multiple frequency bands using chirped train signals,” submitted to *IEEE Trans. on Geoscience and Remote Sensing*.

References

- [1] E. Bleszynski, M. Bleszynski, T. Jaroszewicz, and R. Albanese, “Analysis of dispersive effects and enhanced medium penetrability in wide-band pulse propagation through sparse discrete media,” *IEEE Transactions on Antennas and Propagation*, vol. 60, pp. 3265–3277, 2012.
- [2] E. H. Bleszynski, M. C. Bleszynski, T. Jaroszewicz, and R. Albanese, “Imaging through obscuring, discrete-scatterer media with chirped trains of wide-band pulses,” *IEEE Transactions on Antennas and Propagation*, vol. 61, pp. 310–319, 2013.
- [3] E. H. Bleszynski, M. K. Bleszynski, and T. Jaroszewicz, “Amplification of signal intensity in imaging through discrete random media through signal interference gating and the use of mutual coherence function,” in *Ultra-Wideband, Short-Pulse Electromagnetics 10*. Springer, 2014, pp. 89–99.
- [4] E. Bleszynski, M. Bleszynski, and T. Jaroszewicz, “Early-time diffusion in pulse propagation through dilute random media,” *Optics Letters*, vol. 39, no. 20, pp. 5862–5865, 2014.

Appendix A

Imaging with multiple frequency bands using chirped train signals

Elizabeth H. Bleszynski, Marek Ch. Bleszynski, Thomas Jaroszewicz, and Richard Albanese

Abstract—Properties of chirped-train waveforms such as their multi-band power spectra and the resulting point spread and ambiguity functions are described. Possible advantages in the utilization of chirped trains in “multi-spectral” imaging (i.e., imaging based on frequency sub-bands of the chirped train signal) allowing extraction of frequency dependent information with improved signal-to-noise ratio are presented.

Index Terms—chirped train signal, point spread function, ambiguity function, multi-spectral imaging

I. INTRODUCTION

In our previous work [1], [2] we presented an approach to imaging through obscuring media based on a particular form a transmitted waveform – a chirped train signal – i.e., a sequence of identical pulses emitted at linearly varying (chirped) time intervals. The wide-band nature of the pulses was facilitating their penetration through the medium (by means of precursor-type phenomena), while the chirp of the train was providing the frequency bandwidth necessary for achieving the desired range resolution in the image. The latter property of the chirped train was due to its power spectral density containing a structure similar to that of a conventional, continuous, linear-frequency-modulated chirped signal [3].

Chirped train signals are a particular realization of a class of nonuniform pulse trains and have been studied mostly in the context of their range and Doppler (velocity) resolution potential [4], [5], [6], [7].

Here, we concentrate on another feature specific to chirped trains – the existence of “higher harmonics” in the signal power spectrum, i.e., the isolated frequency sub-bands centered approximately at multiples of the chirp fundamental frequency. This property was not relevant in applications we previously considered [2] because of the dominance (due to attenuation in the medium) of the lowest frequency band corresponding to the chirp fundamental frequency.

In this paper we reexamine the problem of the design of chirped-train waveforms in situations where the higher harmonics of the power density spectrum are relevant. We show that under such circumstances it is possible to **redistribute energy** of the signal into several **narrow frequency sub-bands**,

which can be then used to form “spectral images” of lower resolution than those obtained with the full signal bandwidth, but **allowing more efficient extraction of frequency-dependent information** on the material content of the scatterers present on the scene.

It has been shown previously [8] that such images can be obtained by partitioning (in the data processing stage) a wide frequency band of the conventional continuous radar chirp into the desired sub-bands. The chirped train approach proposed here has the potential of enhancing those opportunities: by **splitting the signal spectrum into sub-bands separated by gaps**, one can consolidate, with the same total signal energy, **more energy in the selected sub-bands**, and hence **achieve better signal-to-noise ratios**.

Moreover, since the energy redistribution is controlled by a single parameter of the transmitted waveform – the chirped train bandwidth – one can envisage a data collection scheme alternating between two modes: (i) the **high-resolution imaging mode** utilizing the entire pulse bandwidth, and (ii) the **“spectroscopic” multi-band mode** in which the energy is repartitioned into several separate sub-bands. The mode (i) would provide data for analyzing the scene and identifying spatial areas and objects of interest. Then, the data obtained in mode (ii) could be used to extract further properties of already localized objects.

The analysis of the ambiguity function (AF) of chirped train signals further reveals that while the AF arising in the spectroscopic mode closely resembles the ridge-type structure of the AF of a conventional chirp signal, the AF corresponding to the full-band high-resolution imaging mode exhibits a sheared multi-peak structure which may be of potential interest in Doppler-based target indication.

The paper organized as follows: In Section II we briefly describe a general chirped train signal as a convolution of a function representing a single pulse and another function controlling the distribution of pulses in time. We also discuss the signal main characteristics: in particular its multi-band power density spectrum, the PSF and the AF. Section III concentrates on the selection of parameters of the chirped train waveform of interest in “high-resolution” and “multispectral” imaging modes. An example involving a chirped train signal with rectangularly modulated sinusoidal pulses is presented in Section IV. In Section V possible application of chirped train signals in spotlight synthetic-aperture radar (SAR) imaging with multiple frequency bands is discussed and illustrated by an example. Section VI briefly addresses the experimental

E. H. Bleszynski, M. Ch. Bleszynski, and T. Jaroszewicz are with Monopole Research, Thousand Oaks, CA 91360, U.S. e-mail: elizabeth@monopoleresearch.com.

R. Albanese is with ADED Co, San Antonio, TX 78217, U.S. e-mail: richard.albanese2@gmail.com.

Manuscript received xxx xx, 20xx; revised xxx xx, 20xx.

possibility of forming the desired waveforms. Section VII, Summary, completes the paper.

II. DEFINITION AND PROPERTIES OF A CHIRPED TRAIN SIGNAL

We start with the discussion of the properties of a signal formed by a chirped train of pulses. As we will see, the chirped sequence of pulses can be considered a “discrete analogue” of a conventional continuous chirp pulse, but with a more complex and potentially more useful power density, PSF, and AF structure.

A. Definition of a chirped train of pulses

We consider a signal $F(t)$ composed of a sequence of identical pulses $f(t)$, each of duration T_f , emitted with monotonically decreasing time intervals,

$$F(t) = \sum_{n=-N_g/2}^{N_g/2} f(t - t_n). \quad (1)$$

In analogy to the most common continuous chirp signals, characterized by linear frequency modulation [3], we assume the time instances t_n to be given by¹

$$t_n = \tau_g \left(1 - \beta_g \frac{n}{2N_g} \right) n, \quad (2)$$

or, in other words, the differences between the consecutive intervals to remain constant,

$$(t_{n+1} - t_n) - (t_n - t_{n-1}) = -\frac{\tau_g \beta_g}{N_g}. \quad (3)$$

We call such a signal (1) a chirped train waveform. Without losing generality, but for a greater clarity of expressions, the number of pulses in the train, $N_g + 1$ will be assumed odd (i.e., N_g will be assumed even).

The quantity τ_g in Eqs. (2) and (3) is the average pulse repetition interval. The average pulse repetition frequency (or the train center frequency) is defined as

$$\nu_g := \frac{1}{\tau_g}, \quad (4)$$

where β_g is the frequency modulation parameter. We will denote by T_g the duration of the entire chirped train signal,

$$T_g := N_g \tau_g. \quad (5)$$

An example of the chirped train signal is shown in Fig. 1.

To attach a more physical meaning to the notion of the “train chirping”, we consider a situation when the number of pulses in the train is large, $N_g \gg 1$, and the frequency modulation parameter is small, $\beta_g \ll 1$. Then the time increments between pulses can be expressed as the “derivative” of t_n with respect to n ,

$$t'_n := \frac{dt_n}{dn} = \tau_g \left(1 - \beta_g \frac{n}{N_g} \right), \quad (6)$$

¹ We note that although the formulas (2) and (3), with $\beta_g > 0$, describe an “up-chirp” train, the results of the paper apply equally to both down- and up-chirps.

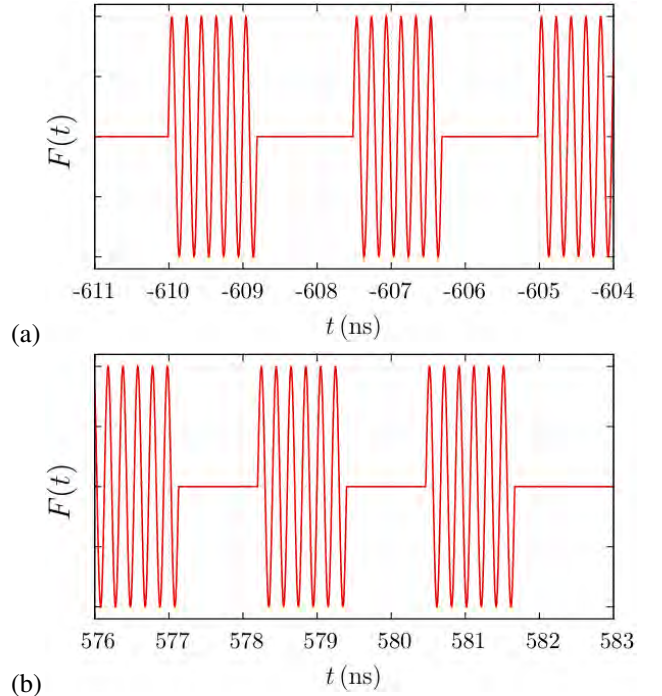


Fig. 1: The first (a) and last (b) few pulses in the chirped train for the problem (b) in Table I.

the instantaneous frequency of the train of pulses can be defined as

$$\nu_n := \frac{1}{t'_n} = \frac{\nu_g}{1 - \beta_g n/N_g} \approx \nu_g \left(1 + \beta_g \frac{n}{N_g} \right), \quad (7)$$

and the chirped train frequency span becomes

$$\nu_{N_g/2} - \nu_{-N_g/2} = \frac{\beta_g \nu_g}{1 - \beta_g^2/4} \approx \beta_g \nu_g =: B_g, \quad (8)$$

where the approximate equality in the last two formulas are valid for $\beta_g \ll 1$. In analogy to the continuous chirp signal, we refer to the quantity B_g as the **bandwidth of the chirped train** and, as indicated by the approximate equality in Eq. (8), the modulation parameter β_g acquires the meaning of a **relative train bandwidth**, $\beta_g = B_g/\nu_g$, i.e., the train bandwidth in the units of the train center frequency.

In our subsequent considerations, we will assume that the pulses in the train do not overlap, i.e., the pulse duration T_f is shorter than the minimum pulse-pulse interval. It follows from (2) that the condition for the pulses not to overlap takes the form:²

$$T_f < t_{N_g/2} - t_{N_g/2-1} = \frac{1}{\nu_g} \left(1 - \beta_g \frac{N_g - 1}{2N_g} \right), \quad (9)$$

which for small bandwidth $\beta_g \ll 1$ simply becomes

$$T_f < \frac{1}{\nu_g}. \quad (10)$$

² The assumption of non-overlapping pulses can be rigorously stated only if the pulses $f(t)$ vanish **exactly** outside their duration intervals. In many practical problems this condition holds only approximately, and the above assumptions have to be relaxed.

In the following, in continuation of the notation of this Section, we will denote quantities associated with individual pulses $f(t)$ in the train with the subscript f and those characterizing properties of the train sequence with the subscript g .

B. Power density of a chirped train signal

It is instructive to represent the chirped train $F(t)$ of Eq. (1) as the convolution

$$F(t) = (g \circ f)(t) , \quad (11)$$

where $g(t)$ is a sequence of delta-functions

$$g(t) = \sum_{n=-N_g/2}^{N_g/2} \delta(t - t_n) . \quad (12)$$

This notation emphasizes the fact that the signal $F(t)$ involves the time profile f of the single pulse, as well as the function g which describes location of pulses in time.

The convolution form (11) of the train implies immediately that its Fourier transform is a product

$$\tilde{F}(\nu) = \tilde{g}(\nu) \tilde{f}(\nu) , \quad (13)$$

with

$$\tilde{g}(\nu) = \sum_{n=-N_g/2}^{N_g/2} e^{2\pi i \nu t_n} \quad (14)$$

and

$$\tilde{f}(\nu) := \int_{-\infty}^{\infty} dt e^{2\pi i \nu t} f(t) . \quad (15)$$

In the following we will always assume that the direct current (DC) component of the pulse vanishes, hence

$$\tilde{f}(0) = \int_{-\infty}^{\infty} dt f(t) = 0 . \quad (16)$$

The quantity directly related to sensing and imaging applications is the power density,

$$W(\nu) := |\tilde{F}(\nu)|^2 = w_g(\nu) w_f(\nu) \quad (17)$$

which, in the case of the chirped train is the product of the power densities of the **train sequence**

$$w_g(\nu) = |\tilde{g}(\nu)|^2 \quad (18)$$

and a **single pulse**

$$w_f(\nu) = |\tilde{f}(\nu)|^2 . \quad (19)$$

We will focus our attention now on the power density $w_g(\nu)$ of the chirped train sequence. We will show that, under some circumstances, the power density spectrum of the chirped train sequence acquires the form of **separate sub-bands** centered approximately at multiples of the chirp train center frequency.³ Further, we will argue how the presence of isolated sub-bands can prove advantageous in a “multispectral” imaging scenario.

³The chirped train power density multi-band structure is due to the discrete nature of the signal.

The power density (18) can be represented as a double sum of the form

$$\begin{aligned} w_g(\nu) &:= |\tilde{g}(\nu)|^2 = \sum_{m,n=-N_g/2}^{N_g/2} e^{2\pi i \nu (t_m - t_n)} \\ &= \sum_{m=-N_g/2}^{N_g/2} \sum_{n=-N_g/2}^{N_g/2} e^{2\pi i \nu \tau_g (m-n) \left[1 - \frac{1}{2} \beta_g (m+n)/N_g\right]} \\ &= \sum_{p=-N_g}^{N_g} \sum_{\substack{q=-(N_g-|p|) \\ \Delta q=2}}^{N_g-|p|} e^{2\pi i \nu \tau_g p \left(1 - \frac{1}{2} \beta_g q/N_g\right)} \\ &\equiv \sum_{q=-N_g}^{N_g} \sum_{\substack{p=-(N_g-|q|) \\ \Delta p=2}}^{N_g-|q|} e^{2\pi i \nu \tau_g p \left(1 - \frac{1}{2} \beta_g q/N_g\right)} , \end{aligned} \quad (20)$$

where in the last expressions we indicated that the sums run over $p \equiv m - n$ or $q \equiv m + n$ with the increments $\Delta p = 2$ or $\Delta q = 2$. The p sum in the last expression of Eq. (20) can be conveniently expressed in terms of the “periodic sinc function”⁴ defined by

$$\text{sinc}_N(z) := \frac{1}{N+1} \sum_{n=-N/2}^{N/2} e^{2\pi i z n/N} = \frac{\sin(\pi \frac{N+1}{N} z)}{(N+1) \sin(\pi \frac{z}{N})} ; \quad (21)$$

if N is odd, the sum here runs over odd-half-integer indices n . An important property of the function $\text{sinc}_N(z)$ is its (anti-)periodicity in z : the relation

$$\text{sinc}_N(z + N) = (-1)^N \text{sinc}_N(z) \quad (22)$$

means that $\text{sinc}_N(z)$ is periodic (for N even) or anti-periodic (for N odd) with the period N .

With the definition (21), Eq. (20) takes the form

$$\begin{aligned} w_g(\nu) &= \sum_{q=-N_g}^{N_g} (N_g - |q| + 1) \\ &\quad \text{sinc}_{N_g-|q|} \left(2(N_g - |q|) \left(1 - \frac{\beta_g q}{2N_g} \right) \frac{\nu}{\nu_g} \right) \\ &= \sum_{j=0}^{N_g} (j+1) \text{sinc}_j \left(2j \left(1 \pm \beta_g \frac{N_g - j}{2N_g} \right) \frac{\nu}{\nu_g} \right) . \end{aligned} \quad (23)$$

In the last expression the “ \pm ” symbol indicates that one has to perform the summation twice, with the “+” and “−” signs; that applies to all terms in the j sum except $j = N_g$, for which the coefficient of β_g vanishes and which enters the sum only once.

We will now use the expression (23) to analyze some of the properties of the power spectrum $w_g(\nu)$, in particular its approximate periodicity in frequency with the period ν_g .

⁴ This function is related to the Dirichlet kernel $D_n(z)$ [9] by $\text{sinc}_N(z) = (N+1)^{-1} D_{N/2}(2\pi z/N)$.

We use the elementary identity⁵

$$\frac{\pi}{\sin(\pi z)} = \sum_{l=-\infty}^{\infty} \frac{(-1)^l}{z-l} \quad (24)$$

to represent the periodic sinc function (21) as

$$\text{sinc}_N(z) = \sum_{l=-\infty}^{\infty} (-1)^{lN} \text{sinc}\left(\frac{N+1}{N}(z-lN)\right), \quad (25)$$

i.e., as an infinite sum of ordinary sinc functions, $\text{sinc}(x) := \sin(\pi x)/(\pi x)$, centered at the multiples of the period N of $\text{sinc}_N(z)$. By substituting (25) in Eq. (23) we find then

$$\begin{aligned} w_g(\nu) &= \sum_{l=-\infty}^{\infty} w_l(\nu) \\ &= \sum_{l=-\infty}^{\infty} \sum_{j=0}^{N_g} (-1)^{lj} (j+1) \text{sinc}\left(2(j+1) \left(\gamma_j^{\pm} \frac{\nu}{\nu_g} - \frac{l}{2}\right)\right) \end{aligned} \quad (26)$$

with

$$\gamma_j^{\pm} := 1 \pm \beta_g \frac{N_g - j}{2N_g}. \quad (27)$$

When inspecting the expression (26) we observe that each w_l is a sum of $N_g + 1$ terms, each term peaked at

$$\nu = \frac{\nu_g}{2\gamma_j^{\pm}} l \quad \text{for } j = 0, \dots, N_g. \quad (28)$$

For a small relative bandwidth β_g , the quantities γ_j^{\pm} become close to unity, and all terms in a given w_l are peaked near the same value ($\nu_g l/2$). Further, for the odd values of l , we expect the terms w_l to be small as the consecutive terms in the j sum change sign and tend to cancel each other. As a result, the power density $w_g(\nu)$ is dominated by terms of **even** l , i.e., by **integer** multiples of the “fundamental” chirp frequency ν_g . Fig. 3, as discussed in more detail in Section III, confirms our predictions.

It can be shown, although we do not present the derivation here, that under the assumptions of a large number of pulses in the train,

$$N_g \gg 1, \quad (29)$$

a small relative bandwidth,

$$\beta_g = B_g/\nu_g \ll 1, \quad (30)$$

and a large time-bandwidth product,

$$b = B_g T_g \quad (31)$$

(where, again, $T_g := N_g \tau_g$ is the signal duration), the exact expression (26) can be well approximated, for $\nu \geq 0$, by

$$\begin{aligned} w_g(\nu) &\approx N_g^2 \text{sinc}^2\left(N_g \frac{\nu}{\nu_g}\right) \\ &+ \frac{\nu_g N_g}{B_g} \sum_{k=1}^{\infty} \frac{1}{k} \text{rect}\left(\frac{\nu - k \nu_g}{k B_g}\right). \end{aligned} \quad (32)$$

⁵ The series here is not absolutely convergent, but can be made so by taking a symmetric limit of a finite sum or by grouping terms, as in [10], Eq. (4.3.93).

Here $\text{rect}(x) = 1$ for $|x| \leq \frac{1}{2}$ and 0 otherwise, and the first term, peaked at $\nu = 0$, is an approximation to the $l = 0$ term in Eq. (26).

The approximate expression (32) has a simple physical interpretation. It represents the spectrum $w_g(\nu)$ as a superposition of the “fundamental harmonic” ($k = 1$) sub-band precisely corresponding to the “Fresnel spectrum” of a conventional chirp signal (centered at ν_g and of bandwidth B_g) and higher-order ($k = 2, 3, \dots$) “harmonics”, each of them approximately rectangular, of width proportional to k , magnitude inversely proportional to k , and centered at

$$\nu_k = k \nu_g. \quad (33)$$

It also follows from the approximate formula (32) that the consecutive harmonics are well separated for harmonic orders

$$k < k_{\max} = \frac{\nu_{\max}}{\nu_g} = \frac{\nu_g}{B_g} = \frac{1}{\beta_g}, \quad (34)$$

and, that at higher frequencies, the harmonics start to overlap. Or, alternatively, the part of the frequency spectrum corresponding to the region of non-overlapping harmonics is

$$0 < \nu < \nu_{\max} = \frac{\nu_g^2}{B_g}. \quad (35)$$

As an example, in Fig. 2 we display power spectral densities of the train sequence ($w_g(\nu)$), the pulse ($w_f(\nu)$), and the full chirped train signal ($W(\nu)$) for parameters listed in Table I. The pulse is assumed to be a rectangularly modulated sinusoid of Eq. (65) (Appendix A), characterized by a frequency ν_f and a duration T_f .

The parameters in this example are chosen in such a way that the first nine harmonics of the train spectrum form isolated sub-bands and the higher harmonics start to overlap. We observe that the rigorously computed power density of the train sequence $w_g(\nu)$, Eq. (26), resembles the pattern predicted by the “rectangular approximation” of Eq. (32). We also observe that the separation of lower harmonics and overlapping of higher harmonics for the rigorously computed power densities follow the predictions of the approximate relation (34).

In example (a) of Fig. 2 the pulse center frequency was chosen in such a way that the pulse power spectrum $w_f(\nu)$ overlaps three isolated harmonics, $k = 4, 5, 6$ of the train spectrum $w_g(\nu)$. As a consequence, the power spectrum $W(\nu)$ of the entire signal, being the product of the two (Eq. (17)), also displays the three distinguishable sub-bands.

The presence of isolated sub-band structures can be of particular interest in multispectral imaging:

- it redistributes energy of the signal in several narrow frequency sub-bands which can be then used in forming “spectral images” providing valuable frequency dependent information on the material content of the scatterers,
- it allows to consolidate, with the same total signal energy, more energy in the selected sub-bands, and hence to achieve a better signal-to-noise ratio.

In Fig. 2(b) we present an example characterized by a similar as before pulse duration T_f , but a higher pulse center frequency ν_f . Now the pulse power spectrum covers the region

TABLE I: Pulse and train parameters used in Fig. 2

example	ν_f (GHz)	T_f (ns)	ν_g (GHz)	B_g (GHz)	N_g
(a)	2.200	0.91	0.420	0.040	500
(b)	5.000	1.20	0.420	0.040	500

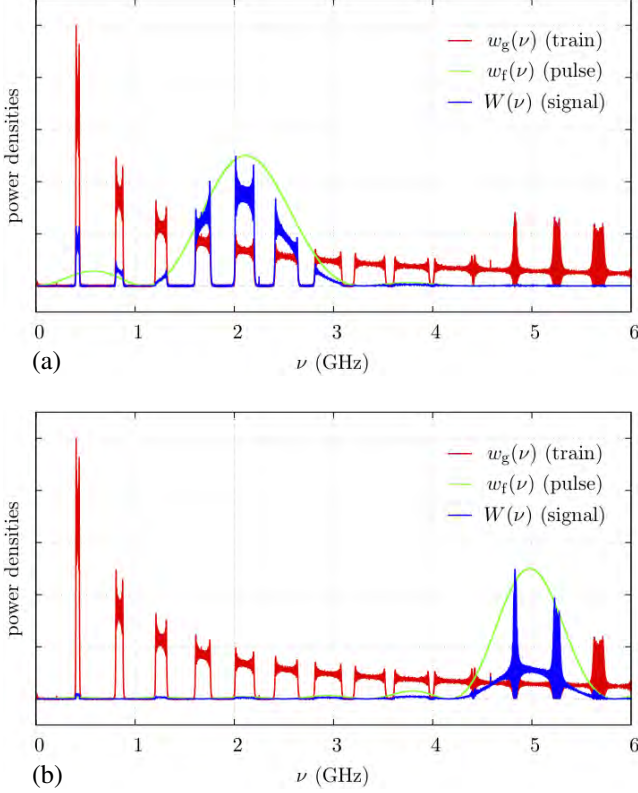


Fig. 2: Power densities of the train sequence ($w_g(\nu)$), the pulse ($w_f(\nu)$), and the full signal ($W(\nu)$), for examples (a) and (b) of Table I. Normalization of the power spectra is arbitrary to facilitate comparison of their shapes.

where the train harmonics start to overlap. In this situation, there are no isolated sub-bands in the power spectrum of the chirped train signal and, as we discuss in more detail in Section IV, the signal acquires properties similar to those of a classical chirp.

The two-mode data collection scheme proposed later in this paper comprises scenarios with both non-overlapping as well as overlapping frequency sub-bands.

C. Point-spread and ambiguity functions of a chirped train signal

In range-based coherent imaging or remote sensing applications based on heterodyne detection the received real signal is converted into in-phase (“I”) and quadrature-phase (“Q”) channels. This operation amounts to forming the *analytic representation* $F_A(t)$ of a real signal $F(t)$, defined as

$$F_A(t) \equiv (AF)(t) := \int_0^\infty d\nu e^{-2\pi i \nu t} \tilde{F}(\nu), \quad (36)$$

i.e., the part of the signal consisting of only positive-frequency Fourier components. Hence, the Fourier transform of the analytic representation $F_A(t)$ is simply

$$\tilde{F}_A(\nu) = H(\nu) \tilde{F}(\nu), \quad (37)$$

where H is the Heaviside step function.⁶

Under the assumption that scattering takes place on a localized point-like target, the received signal $F'(t)$ is proportional to the transmitted signal $F(t)$ delayed by the round-trip time between the transmitter/receiver and the target located at the distance r_0 ,

$$F'(t) = F(t - 2r_0/c). \quad (38)$$

It is well known that in this case the optimal range resolution can be achieved through compression of the received signal by means of the conventional matched-filtering.⁷ This procedure amounts to convolving the analytic representation of the received signal with the time-reversed and translated transmitted signal, and forming the *positive-frequency autocorrelation function* also known as the *point-spread function (PSF)*:

$$\begin{aligned} \chi_F(t - 2r_0/c) &= \int_{-\infty}^{\infty} ds F'_A(s) F_A^*(s - t) \\ &= \int_{-\infty}^{\infty} ds F_A(s - 2r_0/c) F_A^*(s - t) \\ &= \int_{-\infty}^{\infty} ds F_A(s - 2r_0/c) F_A^*(s - t). \end{aligned} \quad (39)$$

We note that, since A is a projection operator, either one or both factors in the above integrands can be the analytic representations of F .

Equivalent and useful expressions for the PSF of the signal $F(t)$ are:

$$\begin{aligned} \chi_F(t) &:= \int_{-\infty}^{\infty} ds F_A(s + \tfrac{1}{2}t) F_A^*(s - \tfrac{1}{2}t) \\ &= \int_0^\infty d\nu e^{-2\pi i \nu t} |\tilde{F}(\nu)|^2 \\ &= \int_0^\infty d\nu e^{-2\pi i \nu t} |\tilde{g}(\nu)|^2 |\tilde{f}(\nu)|^2, \end{aligned} \quad (40)$$

The last equality follows from the fact that the power spectral density of the chirped train signal is the product of the power densities of the train sequence and a single pulse, (17) – (19).

Another important tool in characterizing waveforms is the *time-frequency autocorrelation function* or the *ambiguity function (AF)* [12], [13], [7]. Following the convention of Ref. [13] we define this quantity as

$$\begin{aligned} \chi_F(t, \nu) &:= \int_{-\infty}^{\infty} ds e^{2\pi i \nu s} F_A(s + \tfrac{1}{2}t) F_A^*(s - \tfrac{1}{2}t) \\ &= \int_{|\nu|/2}^{\infty} du e^{-2\pi i u t} \tilde{F}(u + \tfrac{1}{2}\nu) \tilde{F}^*(u - \tfrac{1}{2}\nu). \end{aligned} \quad (41)$$

⁶ Equivalently, the operator A can be expressed in terms of the Hilbert transform H ([11], Ch. 13). We differ from the last reference in defining A as $\frac{1}{2}(I - iH)$, rather than as $I - iH$; therefore, with our definition, A is a projection operator.

⁷ If the signal propagates through a strongly dispersive medium, the appropriate filter may be different than the matched one [2]; here we do not consider medium effects.

The lower limit in the u integral is due to the definition (37) of the analytic representation of \tilde{F} .

The AF is a generalization of the PSF to the case where, as a result of target motion, the received signals are shifted in frequency relative to the transmitted ones. The frequency variable ν represents thus a Doppler shift, and the width of the AF in that variable defines the Doppler resolution of the signal, i.e., its ability of differentiating between objects moving with different (radial) velocities.

Since the pulses in the train are assumed identical, the PSF and the AF of the entire signal $F(t)$ can be expressed in terms of the corresponding functions of the individual pulses $f(t)$ in the train sequence. It follows from Eqs. (40), (41), and (1) that

$$\chi_F(t) = \sum_{m,n=-N_g/2}^{N_g/2} \chi_f(t - (t_m - t_n)) , \quad (42)$$

$$\chi_F(t, \nu) = \sum_{m,n=-N_g/2}^{N_g/2} e^{\pi i \nu (t_m + t_n)} \chi_f(t - (t_m - t_n), \nu) , \quad (43)$$

where

$$\begin{aligned} \chi_f(t) &:= \int_{-\infty}^{\infty} ds f_A(s + \tfrac{1}{2}t) f_A^*(s - \tfrac{1}{2}t) \\ &= \int_0^{\infty} d\nu e^{-2\pi i \nu t} |\tilde{f}(\nu)|^2 \end{aligned} \quad (44)$$

and

$$\begin{aligned} \chi_f(t, \nu) &:= \int_{-\infty}^{\infty} ds e^{2\pi i \nu s} f_A(s + \tfrac{1}{2}t) f_A^*(s - \tfrac{1}{2}t) \\ &= \int_{|\nu|/2}^{\infty} du e^{-2\pi i u t} \tilde{f}(u + \tfrac{1}{2}\nu) \tilde{f}^*(u - \tfrac{1}{2}\nu) \end{aligned} \quad (45)$$

are the PSF and AF of the individual pulse $f(t)$.

Closed-form expressions for the PSF and AF of an individual, rectangularly modulated oscillatory pulse, valid for an arbitrary (in particular small) number of oscillations and, in the case of AF, modified by the addition of frequency windowing, are presented in Appendix A. Eqs. 42 and 43 are subsequently used to numerically evaluate PSF and AF of the chirped train signal. Some examples are presented in detail in Section IV.

We will see that, generally, the PSFs of chirped trains are similar to those of conventional chirped signals. The differences between the AFs of the conventional chirps and the chirped trains are, however, more notable: the latter appear to combine some properties of a conventional chirp signal, favorable in the context of range resolution and “coded” trains of pulses, favorable in Doppler detection of moving objects.

III. DESIGNING THE CHIRPED TRAIN WAVEFORM FOR MULTISPECTRAL IMAGING APPLICATIONS

In Section II we discussed the chirped train waveform and the three main quantities useful in its description: the power density spectrum, the PSF, and the AF. Specifically, we pointed out (Section II-B) that the characteristic isolated sub-band

power density structure of the chirped train signal can be of particular advantage in a “multispectral” imaging scenario.

It is the objective of this Section to specify constraints on the parameters of a chirped train signal which would result in the required sub-band structure of its power density.

We consider a chirped train waveform composed of rectangularly modulated oscillatory pulses characterized by the following parameters: the center frequency, $\nu_f = 1/\tau_f$, the bandwidth, B_f , and the duration $T_f = N_f \tau_f$. The corresponding chirped train parameters are: $\nu_g = 1/\tau_g$, B_g , and $T_g = N_g \tau_g$. In the discussion presented here, we limit ourselves to a situation in which the train parameters ν_g and B_g are already fixed, and we try to determine an appropriate set of parameters characterizing the pulse. Ultimately, more precise bounds on the train and pulse parameters can be derived by formulating an optimization problem.

Our analysis requires that the following conditions are met:

- (i) the signal spectrum contains some non-overlapping sub-bands (harmonics),
- (ii) the spectrum of an individual pulse in the train overlaps the harmonics of interest, and,
- (iii) the pulses in the train do not overlap in time.

As discussed in Section II-B, Eq. (34) the harmonics of order

$$k < k_{\max} = \frac{\nu_g}{B_g} \quad (46)$$

are well separated.

The requirement (ii) that the spectrum of an individual pulse overlaps some separated harmonics of the order k is equivalent to the request that the **pulse center frequency** ν_f is of the order of $k\nu_g$ and smaller than $\nu_{\max} = k_{\max} \nu_g$ or, equivalently,

$$\nu_f \approx k\nu_g < \frac{\nu_g^2}{B_g} . \quad (47)$$

We also require, (iii), that the pulses in the train do not overlap in time, i.e., that the condition (9) holds; this restriction appears natural when the train is generated by repeatedly driving a single source of pulses.

The two conditions, (9) and (47), result in the following **restriction on the number of cycles** in the pulse:

$$N_f = T_f \nu_f < \frac{\nu_f}{\nu_g} \left(1 - \beta_g \frac{N_g - 1}{2 N_g} \right) \approx k \left(1 - \beta_g \frac{N_g - 1}{2 N_g} \right) , \quad (48)$$

with k obeying the inequality (46).

The conditions for the **pulse bandwidth** can be formulated as follows: since the pulse bandwidth cannot be smaller than the inverse of its duration, then,

$$B_f \geq \frac{1}{T_f} > \nu_g \left(1 - \beta_g \frac{N_g - 1}{2 N_g} \right) . \quad (49)$$

Further, the center frequency ν_f of the individual pulse in the train (understood as a position of the maximum in its spectrum) cannot be lower than its bandwidth, hence

$$\nu_f \geq B_f > \nu_g \left(1 - \beta_g \frac{N_g - 1}{2 N_g} \right) . \quad (50)$$

TABLE II: Pulse and train parameters used in the examples

case	ν_f (GHz)	T_f (ns)	ν_g (GHz)	B_g (GHz)	N_g
(a)	2.200	0.91	0.420	0.040	500
(b)	2.200	0.91	0.420	0.090	500

Eqs. (50) and (47) lead to the following useful relation

$$B_f > kB_g \left(1 - \beta_g \frac{N_g - 1}{2N_g} \right). \quad (51)$$

From the point of view of imaging, range resolution is an important parameter. Since the widths of the sub-bands are, approximately, given by kB_g , therefore the expected range resolution for a single sub-band is

$$\Delta r = \frac{c}{2kB_g} \equiv \frac{c\nu_g}{2\nu_f B_g}. \quad (52)$$

With the harmonic orders limited by (34), the best attainable resolution (for $k \lesssim k_{\max} = \nu_g/B_g$) is

$$\Delta r_{\min} \gtrsim \frac{c}{2\nu_g}. \quad (53)$$

Another observation is in order here. As the energy redistribution is controlled by a single parameter of the transmitted waveform – the chirped train bandwidth – one can envisage a data collection scheme alternating between two modes: (i) the **high-resolution imaging mode** utilizing the entire pulse bandwidth, and (ii) the **“spectroscopic” multi-band mode** in which the energy is repartitioned into several separate sub-bands. The mode (i) would provide data for analyzing the scene and identifying spatial areas and objects of interest. Then, the data obtained in mode (ii) could be used to extract further properties of already localized objects.

IV. EXAMPLES OF CHIRPED TRAIN WAVEFORMS AND THEIR PSFs AND AFS

To illustrate the behavior of a propagating chirped train signal we consider examples in the radar domain.

Parameters of the chirped train signal, i.e. parameters of the single pulse and the chirped train, are given in Table II. Parameters in case (a) were chosen to approximately reproduce the total frequency band of the measurements of Ref. [8]. Case (b) is characterized by an increased chirped train bandwidth B_g .

The pulse carrier frequency in both cases was chosen such that its power density spectrum overlaps the 4th, 5th, and 6th harmonics of the chirped train.

We start our discussion with case (a):

- The power densities, $w_g(\nu)$, $w_f(\nu)$ and $W(\nu)$, corresponding to this case are plotted in Fig. 3(a).
- PSFs representing the **windowed** harmonics, $k = 4$, $k = 5$, and $k = 6$, are plotted in Fig. 4. We note that the widths of these distributions and hence the resulting range resolutions are in agreement with the predictions of Eq. (52).

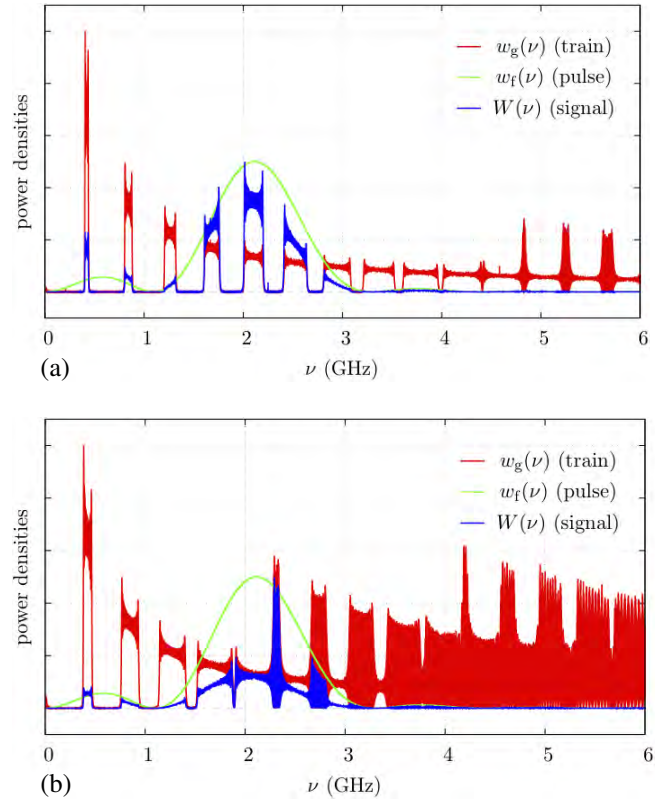


Fig. 3: Power densities of the train sequence ($w_g(\nu)$), the pulse ($w_f(\nu)$), and the full signal ($W(\nu)$), for the examples (a) and (b) of Table II. Normalization of the power spectra is arbitrary to facilitate comparison of their shapes.

- In Fig. 5 the power spectrum $W(\nu)$ (the same as in Fig. 3(a)) is compared with the power spectrum $W_c(\nu)$ of the “equivalent” conventional chirp characterized by the parameters

$$\nu_c = 2.12 \text{ GHz}, \quad T_c = 1,190 \text{ ns}, \quad B_c = 1.08 \text{ GHz}, \quad (54)$$

where the equivalence is meant in the sense of the same duration, approximately the same total bandwidth, and **the same total energy** (i.e., integrated power density) of the signals.⁸

We find (Fig. 5) that **while the energy in the conventional chirp is uniformly spread over the entire bandwidth, in the chirped train it is concentrated in several separate sub-bands.**

The observed energy distribution of the chirped train signal may have important and desirable consequences. In particular, the separated frequency sub-bands may be used more effectively in situations where we are interested in detecting effects of material dispersion or identifying material properties of the scatterer.

If the conventional chirped signal $W_c(\nu)$ of Fig. 5 were to be used for the purpose of identifying material properties then, in the data processing stage, one would have to partition the 1 GHz frequency band into, e.g. 5 sub-bands and, for each of

⁸ These conditions imply that the train and conventional chirp signal amplitudes are different.

the sub-bands create an image using approximately 1/5-th of the total signal energy.

Using the chirped train signal ($W(\nu)$ in Fig. 5), on the other hand, one can utilize a smaller number (here 3) of more widely separated sub-bands, each containing a larger amount of energy and thus providing a better signal-to-noise (S/N) ratio. The gain due to higher S/N ratio may compensate for the absence of some frequency intervals, especially if we are interested in image differences for more widely spread frequencies.

A note is in order here. There is a price for utilizing the individual sub-bands of the chirped train signal. It is the same price one has to pay when partitioning a conventional chirp: while utilizing the full signal bandwidth gives rise to a high resolution (about 1.0 GHz in the discussed example, corresponding to the spatial resolution of about 15 cm), using frequency sub-bands of a chirped train signal causes resolution deterioration to about 75 cm.

However, using the chirped train waveform poses an interesting possibility to alleviate the above mentioned drawback. Parameters chosen in case (a) led to the segmented power spectrum with non-overlapping harmonics. Changing just one parameter – increasing the train chirp bandwidth B_g from 0.040 GHz to 0.090 GHz (case (b)) – causes the harmonics to start overlapping. The resulting power distribution is shown in Fig. 6. But it is Fig. 7, the plot of the corresponding PSFs, which we would like to comment on in more detail. We observe that power density spectrum with isolated, non-overlapping sub-bands gives rise to PSF with very high side-lobes (which effectively would lead to a significant image deterioration). However, the chirped train signal with overlapping sub-bands and the conventional chirp signal, in spite of very different power density distributions, result in closely similar PSFs. Therefore, both signals provide nearly identical high resolution of about 15 cm when the imaging process utilizes the frequency bandwidth

$$B_w = 2.66 \text{ GHz} - 1.58 \text{ GHz} = 1.08 \text{ GHz} \quad (55)$$

approximately equal to the pulse bandwidth B_f . We also observe that the total signal energy within the window is reduced rather insignificantly (approximately by 20%).

The above observations suggest a particularly attractive measurement scenario of alternating (perhaps instantly) between the two modes:

- (i) the **full-band high-resolution mode** utilizing the bandwidth B_w , approximately equal the pulse bandwidth B_f (Figs. 3(b) and 6), and,
- (ii) the **“spectroscopic”, multi-band mode** in which the energy is repartitioned into several separate sub-bands, as visualized in Figs. 3(a) and 5.

The first mode would provide a high temporal (and thus spatial) resolution, while the second would offer a more detailed spectral information however, with a lower resolution. In order to switch between these modes one would only need to **change a single parameter**: the train chirp bandwidth B_g .

We also note that the scenario discussed above could be easily modified in various other ways. Since the constraints

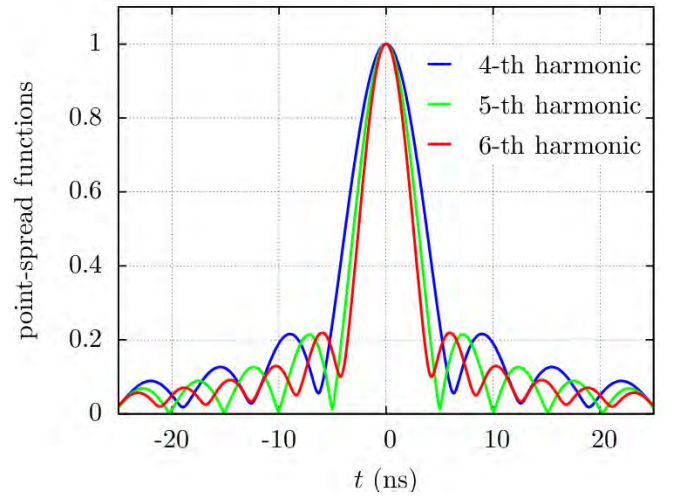


Fig. 4: Absolute values $|\chi_F(t)|$ of the point-spread functions for the three selected frequency sub-bands in Fig. 3(a), normalized to unity at the peak.

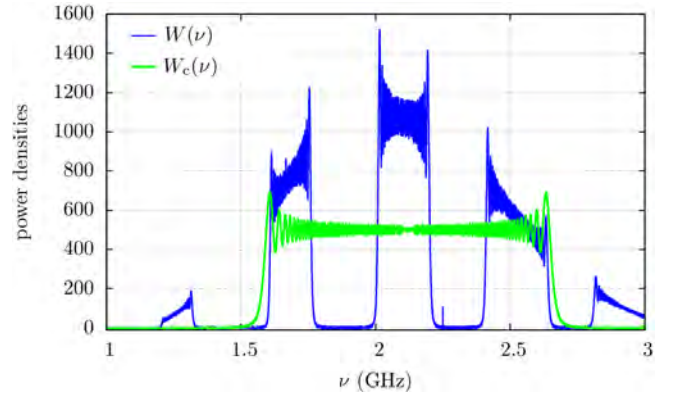


Fig. 5: Power spectrum $W(\nu)$ of the chirped train with bandwidth $B_g = 0.040$ GHz (Table II (a)) compared to the spectrum $W_c(\nu)$ of the “equivalent” conventional chirped signal (54), with the same total energy, duration, and total bandwidth.

(50) and (48) provide considerable latitude in choosing the waveform parameters, one could design signals with more or fewer sub-bands, with better equalized sub-band energies, lower or higher harmonic orders, etc. These variations might offer interesting possibilities of novel applications in radar sensing and imaging.

To complete the discussion of the described two-mode scenario we will present examples of the respective AFs of the chirped train signal.⁹

First we concentrate on the problem of the spectroscopic, multi-band mode (ii) characterized by non-overlapping harmonics (Table II, case (a)) and, subsequently on the full-band high-resolution mode (i) characterized by the parameters of

⁹Trains of non-uniformly spaced pulses (including linearly varying intervals) have been analyzed in Ref. [4]. However, the main purpose of that analysis was to form thumbtack-type AFs, and trains with linear interval variation have not been identified as a distinct class of waveforms.

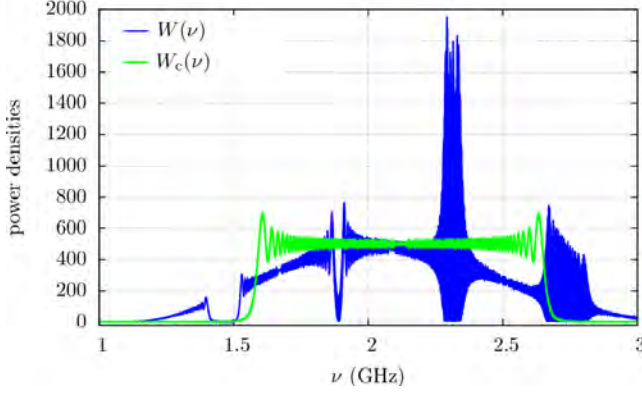


Fig. 6: Power spectrum $W(\nu)$ of the chirped train with an increased train bandwidth $B_g = 0.090$ GHz (Table II (b)), hence nearly or partly overlapping harmonics, compared, for reference, to the same conventional chirp spectrum $W_c(\nu)$ of (54).

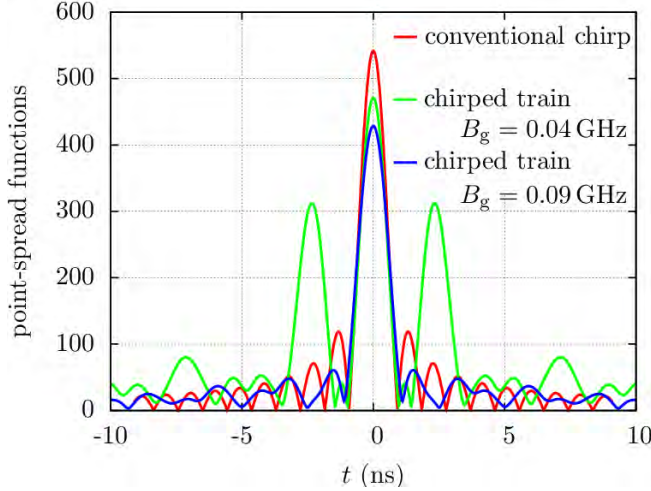


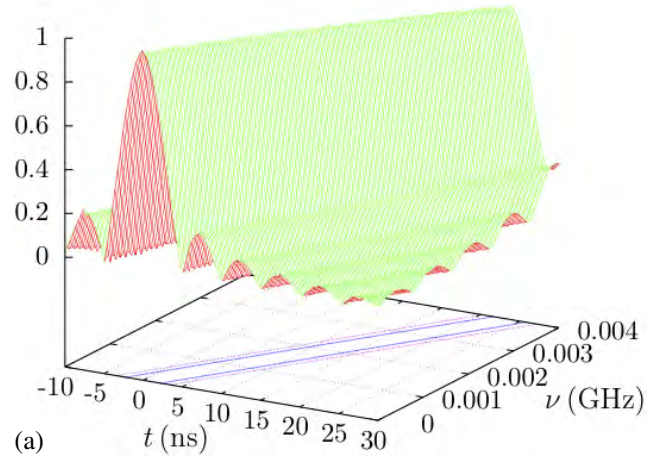
Fig. 7: Absolute values of the point-spread functions corresponding to the conventional chirp and the chirped train power spectra of Figs. 5 and 6. All the PSF are computed with a rectangular frequency window from 1.58 to 2.66 GHz and their values at $t = 0$ represent the total signal energies within the window (assuming unit energy of a single pulse in the train).

Table II, case (b).

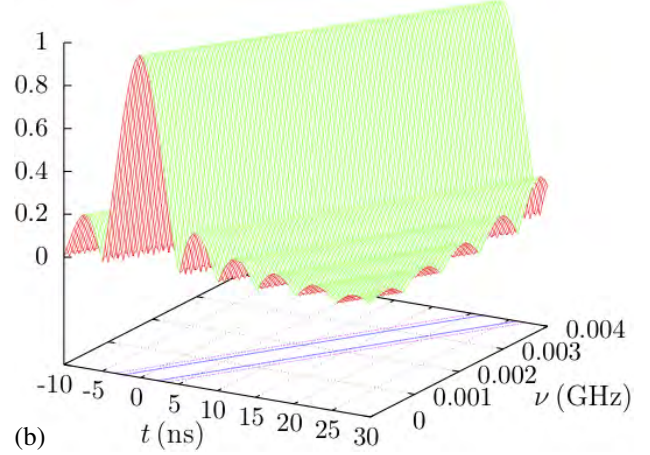
One of the AFs arising in the spectroscopic, multi-band case of non-overlapping harmonics is shown in Fig. 8(a); this AF is computed for the central, 5th harmonic, windowed in frequency in the same way as the corresponding PSF in Fig. 4. As expected, the AF corresponding to this single separated frequency sub-band closely resembles the ridge-type structure of the AF of a classical chirp (e.g., [7], Ch. 4.2). To visualize this similarity, in Fig. 8(b) we plot AF of a classical chirp characterized by the parameters

$$\nu_c = 2.12 \text{ GHz}, \quad T_c = 1,190 \text{ ns}, \quad B_c = 0.20 \text{ GHz}, \quad (56)$$

i.e., by the power spectrum which, with a very good approx-



(a)



(b)

Fig. 8: Plots of the AF for the chirped train signal, case (a) of Table II, computed with a frequency window covering the 5th harmonic (top), compared to the approximately equivalent conventional chirp with the parameters given by Eq. (56) (bottom).

imation, can be considered equivalent to the power spectrum of the 5th harmonic of the considered chirped train signal.

As the next example we discuss the AF corresponding to the case of overlapping harmonics (Table II, case (b)). The AF computed, in analogy with the PSF of Fig. 7, with the effective bandwidth of $B_w = 1.08$ GHz, is presented in Figs. 9 and 10. Again, for the quantitative comparison, we also plot there the AF of the “equivalent” classical chirp (with parameters specified in (54)).

In order to facilitate the visualization and the discussion, the AFs are shown in two different frequency ranges: a larger range (up to 0.6 GHz) and a much smaller range (up to 0.008 GHz). The latter scale is comparable to the Doppler resolution than can be achieved with the considered signal.

We observe that the time resolutions Δt in the AFs for the chirped train signal and the equivalent classical chirp are given by the inverse of the effective frequency bandwidths ($1/B_w$ and $1/B_c$). Also, in both cases, the Doppler-frequency resolutions $\Delta \nu$ are inversely proportional to the total signal durations ($1/T_g$ and $1/T_c$). For the classical chirp, the above

estimates are fully compatible with the estimates of [7].

However, as seen from the Figures, the overall structures of the AFs of the conventional chirped signal and the high-resolution-mode chirped train are entirely different. As is well known (e.g., [7], Ch. 4.2) and as we observed in the example discussed above (Fig. 8), the AF of a classical chirp exhibits a ridge along

$$\frac{\nu}{t} \approx \frac{B_c}{T_c} \quad (\text{classical chirp}) ; \quad (57)$$

the slope in the above relation represents the linear-frequency-modulation “shear” effect. This feature is clearly seen in Figs. 9(c) and 10(c), as well as 8(b).

On the other hand, the AF of the chirped train signal consists of rows of isolated peaks.¹⁰ This behavior is similar to that of a *uniformly-spaced* coherent train of identical pulses ([7], Ch. 4.3). In particular, as marked in Fig. 10(a), the time spacing between the peaks is about $\tau_g = 1/\nu_g$ and the frequency spacing is ν_g . There are infinitely many rows of peaks distributed periodically in ν , but progressively weaker with the increasing Doppler frequency. However, the *chirped* train signal results in the rows being slanted (*sheared*) by the amount proportional to the chirp bandwidth. The analysis of Appendix B shows that the slope ν/t of the shear is

$$\frac{\nu}{t} \approx \frac{\nu_f B_g}{\nu_g T_g} \quad (\text{chirped train}) . \quad (58)$$

Further, Eqs. (57) and (58), as well as the estimates indicated in Fig. 10, show that:

- 1) The narrow peak (time resolution $\Delta t \approx 1/B_w$) of the PSF of the chirped train $\chi_F(t) = \chi_F(t, \nu = 0)$ can be attributed to the fact that only one AF peak (at $t = \nu = 0$) remains on the t axis, and the remaining ones are shifted in frequency as a result of “shearing”. The requirement that the remaining peaks are absent from the PSF (i.e., from the $\nu = 0$ axis) is that the frequency shift of the peak located at $t \approx \tau_g$ is larger than its width, i.e., from Eq. (58) and Fig. 10(b),

$$\frac{\nu_f B_g}{\nu_g^2 T_g} > \frac{1}{T_g} . \quad (59)$$

This condition is equivalent to

$$\frac{\nu_f}{\nu_g} B_g > \nu_g . \quad (60)$$

Since $\nu_f/\nu_g \approx k$ is, approximately, the train harmonic number k in the considered frequency window $[\nu_1, \nu_2]$, the last condition means that the harmonic width kB_g is larger than the inter-harmonic spacing ν_g ; in other words, the harmonics *overlap*.

- 2) The AFs in Figs. 9(a,b) and 10(a,b) represent signals for which the pulse bandwidth B_f exceeds the inter-harmonic frequency spacing ν_g . In this case the peaks in each row of the AF are separated, because $1/B_f < 1/\nu_g \equiv \tau_g$. As soon as B_f decreases below ν_g , the peaks start to overlap and start to form an increasingly smooth

ridge, i.e., the AF of the train becomes more similar to that of a classical chirp.

- 3) In our example, when we reduce the chirp bandwidth B_g to a value for which the harmonics about ν_f do not overlap and window only one harmonic (frequency sub-band), we have $B_c \approx (\nu_f/\nu_g) B_g$ and, since $T_c = T_g$, the shear slopes (57) and (58) become identical.

To summarize, in the full-band “high-resolution mode”, when the pulse spectrum and the selected frequency window extend over several overlapping train harmonics, the chirped train AFs exhibit some significant differences compared to those of the “equivalent” classical chirp. The most striking contrast is the appearance of separate peaks in the chirped train signal, as opposed to a continuous ridge for the classical chirp. This feature may reduce continuous time-frequency ambiguities to discrete ones, and thus offer advantages in Doppler-based object indication.

V. SAR IMAGING WITH CHIRPED TRAINS OF PULSES

We consider now the chirped train signal in the context of spotlight synthetic-aperture radar (SAR) imaging.

For definiteness, we assume in the following that the spectrum of the received signal, reflected from the scene, has been windowed to some frequency band $[\nu_0 - B_0/2, \nu_0 + B_0/2] \equiv [\nu_{\min}, \nu_{\max}]$; it may contain one or more harmonics of the train chirp. The scene is located on the $z = 0$ plane and centered at the origin $\mathbf{0}$. We assume the scene contains J stationary point scatterers located at points $\boldsymbol{\rho}_j = (x_j, y_j)$ on the scene plane and characterized by isotropic complex reflectivities A_j . The scene is being observed from an aperture $\gamma(\theta)$ located in a horizontal plane, parameterized by the azimuthal angle θ measured relative to the scene center and defined by the angular interval $[\theta_{\min}, \theta_{\max}]$ of size $\Theta = \theta_{\max} - \theta_{\min}$. The signal $F(t)$ is being emitted and the reflected signal received¹¹ at aperture points θ_s , $s = 1, \dots, S$. The received signals are being recorded as functions of time at all aperture points and the resulting phase history is used to form the image of the scene. According to the conventional time-domain back-projection procedure [14], [15], [16], the complex image amplitude u , as a function of a scene point $\boldsymbol{\rho}$, is given by¹²

$$u(\boldsymbol{\rho}) = \frac{1}{S} \sum_{s=1}^S \sum_{j=1}^J A_j \chi_F(T_j(\boldsymbol{\rho}, \theta_s)) = \sum_{j=1}^J A_j u_j(\boldsymbol{\rho}) , \quad (61)$$

where

$$u_j(\boldsymbol{\rho}) = \frac{1}{S} \sum_{s=1}^S \chi_F(T_j(\boldsymbol{\rho}, \theta_s)) \quad (62)$$

is the image amplitude due to the j -th scatterer, and

$$T_j(\boldsymbol{\rho}, \theta) = \frac{2}{c} (|\gamma(\theta) - \boldsymbol{\rho}| - |\gamma(\theta) - \boldsymbol{\rho}_j|) \quad (63)$$

is the difference in the signal round-trip travel times between the SAR platform and the image and scatterer location points.

¹¹ We adopt the “stop-go” approximation, justified in airborne SAR.

¹² We omit here various propagation-related factors, which are not essential in analyzing the image resolution. We also omit the SAR phase-history processing details related to extracting rapid phase variation associated with the scene center.

¹⁰ By rows we mean sequences of peaks aligned with the t axis, while columns are aligned with the ν axis.

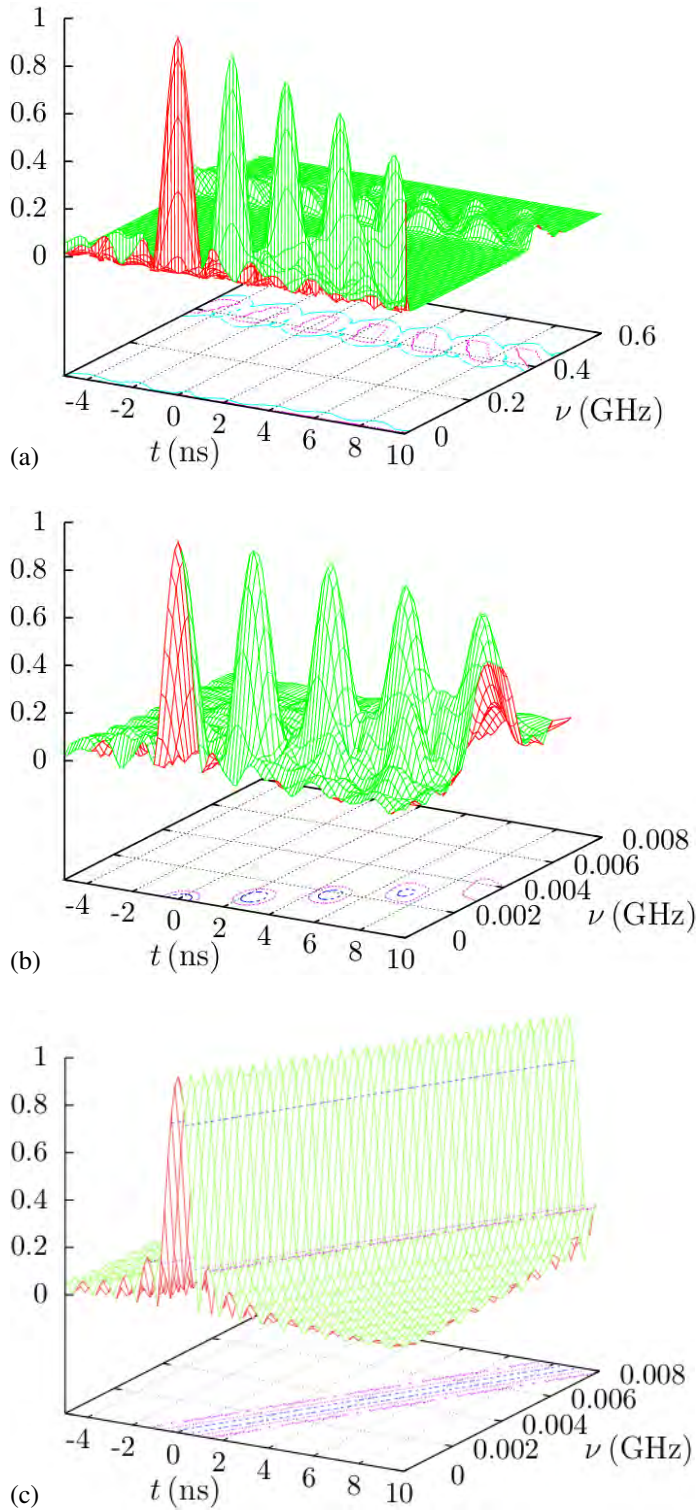


Fig. 9: Absolute values of the AF for the chirped train signal with overlapping frequency bands, Table II, case (b), (top and middle), and for the approximately equivalent conventional chirp with the parameters of Eq. (54) (bottom).

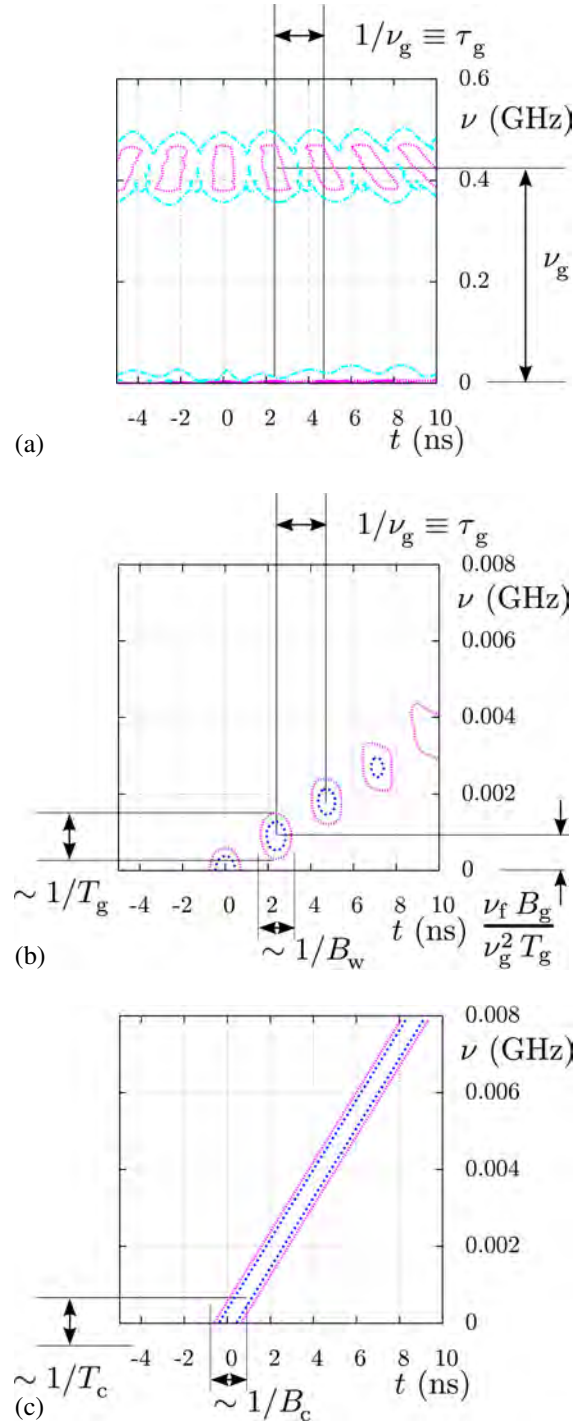


Fig. 10: Contour plots of the AFs corresponding to Fig. 9.

The expression (61) can be immediately used to form the image $u(\rho)$ in terms of the known PSFs χ_F of the signal and the assumed SAR trajectory $\gamma(\theta)$.

As an example of SAR imaging utilizing frequency sub-bands of signals composed of chirped trains of pulses we consider signals (a) and (b) from the Table II and form images in the “spectroscopic” and “high-resolution” modes; in the spectroscopic mode we concentrate on the sub-band corresponding to the signal’s fifth harmonic, $k = 5$.

We consider a simulated scene consisting of $J = 4$ point scatterers of identical reflectivities (assumed to be $A_j = 1$) located at $\rho_2 = (0, 0)$, $\rho_2 = (3.0 \text{ m}, 0)$, $\rho_3 = (0, 3.0 \text{ m})$, and $\rho_4 = (6.0 \text{ m}, 6.0 \text{ m})$. Finally, we assume a synthetic aperture $[\theta_{\min}, \theta_{\max}] = [-3^\circ, 3^\circ]$ at the elevation angle $\beta = 45^\circ$. For the purpose of forming an image, the distance R between the scene and the SAR platform is irrelevant, as long as $R > L^2/\lambda_f$, where L is the scene size and λ_f is the wavelength corresponding to the pulse center frequency. In our case $L = 7 \text{ m}$ and $\lambda_f \approx 0.13636 \text{ m}$, so this condition amounts to $R > 360 \text{ m}$.

The estimates of down-range and cross-range resolutions are

$$\mathcal{R}_d = \frac{c}{2k B_g \cos \beta}, \quad \mathcal{R}_c = \frac{\lambda_f}{2\theta \cos \beta}. \quad (64)$$

With our parameters, we obtain resolutions $\mathcal{R}_d \approx 1.06 \text{ m}$ and $\mathcal{R}_c \approx 0.92 \text{ m}$.

Images are formed by using the time-domain back-projection formula (61) directly. According to the Nyquist sampling criteria, the minimum required number of (uniformly distributed) aperture points is $S \approx L/\mathcal{R}_c$. For our very small “scene”, just a few points ($S \gtrsim 7$) would be sufficient; however, in the computations we take the number of aperture points $S = 61$ (spaced by 0.1°), appropriate for a more typical scene patch of size $L \approx 50 \text{ m}$.

Fig. 11(a) shows the resulting image obtained in the spectroscopic mode, based on the fifth harmonic sub-band of the spectrum. In agreement with the estimates (64), it has approximately the same resolution in the vertical (cross-range) and horizontal (down-range) directions. The images of the scatterers have relatively high sidelobes in both directions. These sidelobes could have been easily reduced by applying smooth windowing in the angle and frequency. However, in order not to introduce unnecessary image modifications, we used the back-projection formula (61) literally, without any additional filtering.

Fig. 11(b) shows the image of the same scene obtained in the high resolution mode. As anticipated, we observe the significantly improved range resolution. We note that the azimuthal resolution could be improved by increasing the aperture size.

VI. A POSSIBLE REALIZATION OF CHIRPED TRAIN SIGNAL GENERATION

Recent technological advances in programmable waveform generators, especially those based on the field-programmable gate arrays (FPGAs) make it possible to realize a wide variety of signal shapes (e.g., [17], [18]), in particular the chirped-train type signals discussed here.

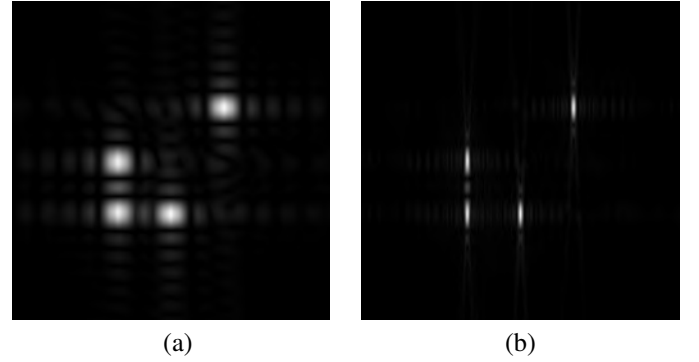


Fig. 11: Intensity images, $|u(\rho)|$, obtained in the “spectroscopic” (a) and “high-resolution” (b) modes. The horizontal (x) and vertical (y) axes correspond to the down- and cross-range directions.

A scenario can be considered in which the transmitting antenna is driven by an *arbitrary waveform generator* (AWG) and an appropriate wide-band amplifier. For example, the generating device could be AWG 7122B manufactured by Tektronix, Inc. According to the data sheet of this instrument, it is able to generate long complex waveforms in the frequency range up to 9.6 GHz with the bandwidth of up to 5.3 GHz. The extended-memory model can store a sequence of $64 \cdot 10^6$ sample points.

VII. SUMMARY

The main subject of this work was the analysis of properties of a particular type of a waveform – a chirped train of short pulses. The theoretical analysis and examples indicate that such waveforms exhibit a number of interesting features which may prove useful in radar imaging scenarios:

- 1) The discrete nature of the train consisting of pulses emitted at linearly varying (chirped) time intervals and the average repetition frequency ν_g gives rise to spectra, such as shown in Fig. 3, which involve a quasi-periodic sequence of frequency bands centered at integer multiples $k\nu_g$ (with $k = 1, 2, \dots$) of the “fundamental frequency” ν_g .
- 2) The widths of the frequency bands are controlled by the chirp bandwidth B_g of the train and grow proportionally to the “harmonic order” k .
- 3) Superimposed on that spectrum is the power distribution of a single pulse. Since the pulses are assumed not to overlap, their duration is limited and their bandwidth B_f cannot be smaller than the train repetition frequency ν_g (Eq. (50)).

The feature 3) indicates that the pulse spectrum may overlap more than one harmonic (Figs. 3(a) and (b)). At the same time, the properties 1 and 2 allow manipulating the train structure so that the resulting spectrum of the full signal may vary from a quasi-continuous wide-band distribution to a distribution exhibiting separate non-overlapping sub-bands. These widely different spectra may be used in different imaging scenarios, such as high-resolution imaging mode utilizing the entire

pulse bandwidth vs. multi-spectral or material-identification imaging mode with lower resolution determined by the widths of consecutive sub-bands. In addition, in the multispectral mode, the signal energy is concentrated in several separate sub-bands, each containing a larger energy fraction than a partitioned, “equivalent”, conventional chirped signal, hence a better signal-to-noise ratio can be obtained. The ability of utilizing programmable waveform generators and switching between the two modes (perhaps on-the-fly, during the measurements) by varying just one waveform parameter, the chirped train bandwidth B_g , may render realization of the proposed technique practical.

In addition, the appearance of separate peaks in the AF of chirped train signal as opposed to a continuous ridge for the classical chirp, may reduce continuous time-frequency ambiguities to discrete ones, and thus offer advantages in Doppler-based object indication.

The main emphasis in the present work was on the structure of the train of pulses, its spectrum, and its significance in imaging and remote sensing. At this stage we did not include attenuation or jitter effects. Both types of effects can be included in our analysis in a relatively straightforward way and will constitute the content of future papers.

APPENDIX A

PSF AND AF FOR A CHIRPED TRAIN SIGNAL COMPOSED OF RECTANGULARLY MODULATED OSCILLATORY PULSES

We analyze here an example of a chirped train signal composed of *rectangularly modulated oscillatory pulses*. We obtain analytic expressions for the single-pulse PSF and AF which are valid for an arbitrary (in particular small) number of oscillations. They are then used to build the PSF and AF of the chirped train signal, and applied in the examples presented in Sections IV and V.

PSF $\chi_f(t)$ of a rectangularly modulated oscillatory pulse. We assume a rectangularly modulated oscillatory pulse

$$f(t) = \frac{2}{\sqrt{T_f}} \text{rect}\left(\frac{t}{T_f}\right) \sin(2\pi \nu_f t) \quad (65)$$

with an integer number $N_f = \nu_f T_f$ of cycles, which ensures vanishing of the DC component of the signal. For definiteness, the pulse $f(t)$ is defined to have unit L^2 norm (unit positive-frequency “energy”), which corresponds to

$$\chi_f(0) = \int_0^\infty d\nu |\tilde{f}(\nu)|^2 = 1. \quad (66)$$

The Fourier transform of the pulse (65) is

$$\begin{aligned} \tilde{f}(\nu) &= i\sqrt{T_f} [\text{sinc}(T_f(\nu - \nu_f)) - \text{sinc}(T_f(\nu + \nu_f))] \\ &= \frac{i}{\pi} (-1)^{N_f-1} \frac{2}{\sqrt{N_f \nu_f}} \frac{\nu_f^2}{\nu_f^2 - \nu^2} \sin(\pi T_f \nu), \end{aligned} \quad (67)$$

which specifies the pulse effective bandwidth $B_f = 1/T_f = \nu_f/N_f$. We reiterate that the absence of the DC component ($f(0) = 0$) implies that the integral of the PSF $\chi_f(t)$ vanishes.

The PSF $\chi_f(t)$ (Eq. (44)) of the pulse, defined by Eq. (65), can be expressed in terms of the sine and cosine integrals $\text{Si}(x)$

and $\text{Ci}(x)$ ([10], Ch. 5). The result is

$$\chi_f(t) = \frac{i}{2\pi^2 N_f} \{X_{N_f}(t) + X_{-N_f}(t) - 2X_0(t)\}, \quad (68)$$

where

$$\begin{aligned} X_N(t) &= [\sin(2\pi \nu_f t) - 2\pi(\nu_f t - N) \cos(2\pi \nu_f t)] \text{Ci}(2\pi(\nu_f t - N)) \\ &\quad - [\cos(2\pi \nu_f t) + 2\pi(\nu_f t - N) \sin(2\pi \nu_f t)] \text{Si}(2\pi(\nu_f t - N)), \end{aligned} \quad (69)$$

with $\text{Ci}(-|x|) = \text{Ci}(|x|) - i\pi$. Those expressions can be obtained as a limit of the more general formula (76) for the pulse AF or, alternatively, by using the basic integral ([19], Eq. (3.355.1)),

$$\begin{aligned} &\int_0^\infty dx \frac{1}{(b^2 + x^2)^2} e^{-\mu x} \\ &= \frac{1}{2b^3} \{ \sin(b\mu) \text{Ci}(b\mu) - \cos(b\mu) (\text{Si}(b\mu) - \pi/2) \\ &\quad - b\mu [\cos(b\mu) \text{Ci}(b\mu) + \sin(b\mu) (\text{Si}(b\mu) - \pi/2)] \} \end{aligned} \quad (70)$$

and continuing it analytically to complex μ and negative b^2 , taking into account the logarithmic branch cut of $\text{Ci}(z)$ along the negative real axis. The logarithmic singularities cancel in the sums of Eqs. (68) and (69).

It is well known ([11], [20]) that in the case of a narrow-band (a large number of oscillations) pulse of Eq. (65), the fairly complicated function (68) can be well approximated by the simple expression

$$\hat{\chi}_f(t) = \text{tri}\left(\frac{t}{T_f}\right) e^{-2\pi i \nu_f t}, \quad (71)$$

where $\text{tri}(x) = 1 - |x|$ for $|x| \leq 1$ and 0 otherwise.

Eq. (71) follows from the approximate analytic representation

$$\hat{f}_A(t) = \frac{1}{\sqrt{T_f}} \text{rect}\left(\frac{t}{T_f}\right) e^{-2\pi i \nu_f t}, \quad (72)$$

obtained from Eq. (65) by replacing the factor oscillating with the carrier frequency ν_f with its *approximate* analytic representation

$$\sin(2\pi \nu_f t) \xrightarrow{A} \frac{i}{2} e^{-2\pi i \nu_f t}. \quad (73)$$

(Alternatively, Eq. (71) can be derived from the approximation to Eq. (67), $|\tilde{f}(\nu)|^2 \approx N_f/(\nu_f) \text{sinc}^2(T_f(\nu - \nu_f))$, valid for $|\nu - \nu_f| \ll \nu_f$.) The expression (71) preserves an important property of the original pulse, namely the absence of the DC component.

It is interesting to note (Fig. 12) that $\hat{\chi}_f$ is a good approximation to $\chi_f(t)$ already for small N_f . Even for $N_f = 1$ the deviation $|\hat{\chi}_f(t) - \chi_f(t)|$ does not exceed 0.114, and it is less than 0.02 for $N_f \geq 6$.

AF $\chi_f(t, \nu)$ of a rectangularly modulated oscillatory pulse. We provide here the closed-form expression for the AF of a rectangularly modulated pulse of Eq. (65). The obtained expression is a generalization of Eq. (68) for the PSF.

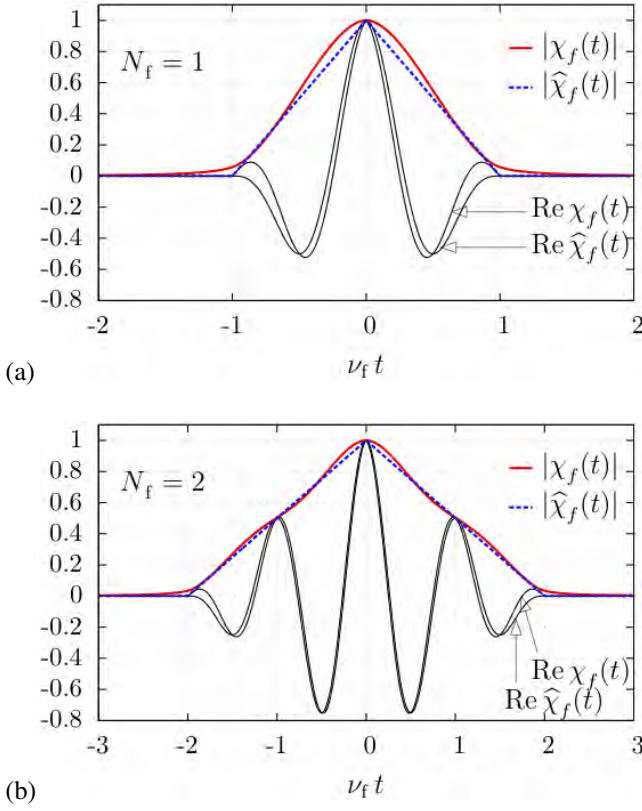


Fig. 12: Real parts and absolute values of the exact, $\chi_f(t)$, and approximate, $\hat{\chi}_f(t)$, PSFs of the rectangularly modulated oscillatory pulse with $N_f = 1$ (a) and $N_f = 2$ (b) oscillations.

We evaluate the AF as defined by Eq. (45) and modified by the addition of a frequency-domain windowing, i.e.,

$$\chi_f(t, \nu; \nu_1, \nu_2) := \int_{\nu_1}^{\nu_2} du e^{-2\pi i u t} \tilde{f}(u + \frac{1}{2}\nu) \tilde{f}^*(u - \frac{1}{2}\nu) \quad (74)$$

for $\frac{1}{2}|\nu| \leq \nu_1 < \nu_2$.

By inserting (65) into (74) and defining the following new variables and parameters,

$$\tau \equiv \nu_f t, \quad \xi \equiv \frac{\nu}{2\nu_f}, \quad x \equiv \frac{u}{\nu_f}, \quad w_{1,2} \equiv \frac{\nu_{1,2}}{\nu_f}, \quad N \equiv N_f, \quad (75)$$

we have

$$\begin{aligned} \chi_f\left(\frac{\tau}{\nu_f}, 2\nu_f \xi; \nu_f w_1, \nu_f w_2\right) &\equiv Y_N(\tau, \xi; w_1, w_2) \\ &= \frac{2}{\pi^2 N} \int_{w_1}^{w_2} dx e^{-2\pi i \tau x} \frac{\sin(\pi N(x + \xi)) \sin(\pi N(x - \xi))}{[(x + \xi)^2 - 1][(x - \xi)^2 - 1]}. \end{aligned} \quad (76)$$

Because of the symmetry relation satisfied by the AF

$$\chi_F(-t, -\nu) = \chi_F^*(t, \nu), \quad (77)$$

we can assume, with no loss of generality, that $\nu \geq 0$ (hence $\xi \geq 0$), and that τ is arbitrary and real. We are thus concerned with the region

$$0 < \xi \leq w_1 < w_2. \quad (78)$$

In the absence of windowing, the lower and upper integration limits are $w_1 = \xi$ and $w_2 = \infty$, corresponding to $\nu_1 = \nu/2$ and $\nu_2 = \infty$.

The integrand of Eq. (76) can be evaluated in a straightforward way, by using the partial-fraction decomposition as well as trigonometric identities, and expressed in terms of the sine and cosine integrals. The individual partial-fraction terms have poles on the integration path. However, since the entire integrand is regular, the integration contour from w_1 to w_2 can be deformed to circumvent the poles in an arbitrary – if only consistent – way. We choose to evaluate the individual terms according to the principal-value prescription. The final expression for the AF assumes then the form

$$Y_N(\tau, \xi; w_1, w_2) = Y_N(\tau, \xi, w_2) - Y_N(\tau, \xi, w_1), \quad (79)$$

where

$$\begin{aligned} Y_N(\tau, \xi, w) &= \frac{1}{16\pi^2 N \xi} \left[\frac{A_N(\tau, 1 + \xi, w)}{1 + \xi} - \frac{A_N(\tau, 1 - \xi, w)}{1 - \xi} \right. \\ &\quad \left. - \frac{A_N(\tau, -(1 + \xi), w)}{1 + \xi} + \frac{A_N(\tau, -(1 - \xi), w)}{1 - \xi} \right] \end{aligned} \quad (80)$$

with

$$\begin{aligned} A_N(\tau, b, w) &= e^{-2\pi i(\tau + N)b} \left[\mathcal{E}i(2\pi\tau(w - b)) \right. \\ &\quad \left. - \mathcal{E}i(2\pi(\tau + N)(w - b)) \right] \\ &\quad + e^{-2\pi i(\tau - N)b} \left[\mathcal{E}i(2\pi\tau(w - b)) \right. \\ &\quad \left. - \mathcal{E}i(2\pi(\tau - N)(w - b)) \right]. \end{aligned} \quad (81)$$

In the last formulae the function $\mathcal{E}i(x)$ is defined, for real x , in terms of the cosine and sine integrals ([10], Ch. 5) as

$$\mathcal{E}i(x) := \text{Ci}(|x|) - i\text{Si}(x); \quad (82)$$

the absolute value of x in Eq. (82) is a reflection of the principal-value definition of the integral (76). Since $\text{Ci}(z)$ has a logarithmic singularity at $z = 0$, evaluating the formulae (79) to (81) also requires some care near the points at which the argument of any of the functions $\mathcal{E}i$ vanishes, to ensure cancellation of the logarithmic terms in their sum.

We note that the expressions (68) – (69) for the (unwindowed) pulse PSF (44) can be obtained from the formula (76) by taking the limits $\nu \rightarrow 0$ (i.e., $\xi \rightarrow 0$), $\nu_1 \rightarrow 0$, and $\nu_2 \rightarrow \infty$. This procedure requires, in particular, expanding the functions $A_N(\tau, b, w)$ in the parameter b , in order to obtain the $\xi \rightarrow 0$ limit of Eq. (80).

As an example, we show in Fig. (13) the AF of the pulse described by the parameters (b) of Table II, with additional frequency windowing. In the absence of windowing, the $\nu = 0$ section of this plot becomes identical to the PSF of Fig. 12(b).

APPENDIX B

DISCUSSION OF PROPERTIES OF THE AF OF CHIRPED TRAINS OF PULSES

We sketch here a derivation of the main properties of the AF of a chirped train of pulses, indicated in Fig. (10) and in Eq. (58).

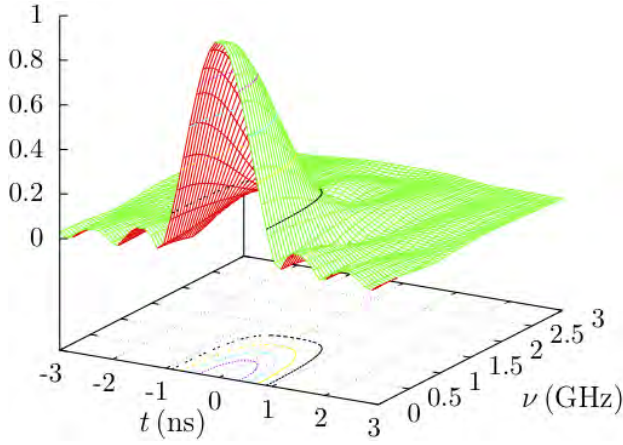


Fig. 13: The absolute value of the AF of a single pulse, with the parameters (b) of Table II, windowed in the frequency interval [1.580 GHz, 2.660 GHz].

Our starting point is the expression (43) for the train AF in terms of the AFs of the individual pulses. In terms of the variables $p \equiv m - n$ and $q \equiv m + n$ we have

$$\chi_F(t, \nu) = \sum_{p, q} e^{\pi i \nu \tau_g [q - \beta_g (q^2 + p^2)/4N_g]} \chi_f\left(t - \tau_g p \left(1 - \frac{\beta_g}{2N_g} q\right), \nu\right), \quad (83)$$

where the summation ranges are as in Eq. (20). We assume a train much longer than the pulse ($N_g \gg 1$) and of a small relative bandwidth ($\beta_g \ll 1$). We are also interested in a “high-resolution” problem, such as the problem (b) of Table II, in which the pulse frequency band covers several partially overlapping harmonics of the signal; this implies, in particular, $\nu_f \approx k \nu_g$ with $k > 1$ ($k = 5$ in the example problem). In addition, we concentrate on a limited domain of the (t, ν) space: (i) $|t| \ll T_g$ and (ii) $|\nu| < \nu_f \approx k \nu_g$. As we will very soon show (and in accordance with the results shown in Figs. 9 and 10), the AF (83) exhibits a lattice of peaks spaced by τ_g and ν_g in the time and frequency directions – similarly to the bed-of-nails AF structure of a uniform train ([7], Ch. 4.3). Further, we will see that each term in the p sum in Eq. (83) generates a row of peaks at $t \approx p \tau_g$. Therefore, the condition (i) implies that $|p| \ll N_g$ and the condition (ii) means that our analysis holds up to about k first rows of peaks in the AF.

Under the above assumptions, the ν -dependence of the pulse AF can be neglected, hence the pulse AF can be replaced with its PSF (44). Therefore, the AF (83) can be approximated by

$$\chi_F(t, \nu) \approx \sum_{p, q} e^{\pi i \nu \tau_g [q - \beta_g (q^2 + p^2)/4N_g]} \int_0^\infty du e^{-2\pi i u [t - \tau_g p (1 - \beta_g q/2N_g)]} |\tilde{f}(u)|^2, \quad (84)$$

which is equivalent to

$$\chi_F(t, \nu) \approx \int_0^\infty du |\tilde{f}(u)|^2 \sum_{p=-N_g}^{N_g} e^{-2\pi i u (t - p \tau_g)} e^{-\pi i \beta_g \tau_g \nu p^2 / 4N_g} \sum_{\substack{q=-(N_g - |p|) \\ \Delta q=2}}^{N_g - |p|} e^{\pi i \tau_g (\nu - p \beta_g \nu_f / N_g) q} e^{-\pi i \beta_g \tau_g \nu q^2 / 4N_g}. \quad (85)$$

In the above expression both the p and q sums depend on the integration variable u . However, the u -dependent phase in the exponent of the q sum vanishes for $p = 0$ and for $p \neq 0$ can be bounded as $|\pi \tau_g \beta_g p q u / N_g| \leq \pi \beta_g \tau_g |p| u$. Since $\beta_g \ll 1$, this u -dependence of the phase is much weaker than in the p -sum, and thus u in the q -sum may be replaced with the center frequency ν_f of the pulse.

Further, since $|\nu| < k \nu_g$, the phase quadratic in p can be bounded by

$$\left| \pi \frac{\beta_g}{4N_g} \tau_g \nu p^2 \right| < \pi k \frac{\beta_g}{4N_g} p^2. \quad (86)$$

Therefore, it is negligible provided

$$|p| \ll \sqrt{\frac{4N_g}{\pi k \beta_g}}; \quad (87)$$

this constraint, which we assume to hold, is stronger than the originally imposed condition $|p| \ll N_g$, but it is still only a very weak restriction.

The above reasoning implies that the AF (85) can be approximated by

$$\chi_F(t, \nu) \approx \int_0^\infty du |\tilde{f}(u)|^2 \sum_p e^{-2\pi i u (t - p \tau_g)} \sum_{q=-N_g, \Delta q=2}^{N_g} e^{\pi i \tau_g (\nu - p \beta_g \nu_f / N_g) q} e^{-\pi i \beta_g \tau_g \nu q^2 / 4N_g} \quad (88)$$

$$= \sum_p \chi_f(t - p \tau_g) S\left(\nu - p \frac{\beta_g \nu_f}{N_g}, \frac{\beta_g \tau_g}{2N_g} \nu\right),$$

with p satisfying the condition (87) and with

$$S(\nu, \kappa \nu) := \sum_{n=-N_g/2}^{N_g/2} e^{2\pi i \nu \tau_g n} e^{-2\pi i \nu \kappa n^2}. \quad (89)$$

Evidently, the factor χ_f in Eq. (88) is responsible for the sequence of peaks in time, of shapes determined by the pulse PSF and spaced by τ_g . Properties of the factor S are less obvious. In the absence of the train chirp ($\beta_g = 0$, hence $\kappa = 0$), it gives rise to a periodic sinc function,

$$S(\nu, 0) = (N_g + 1) \text{sinc}_{N_g}(T_g \nu) \quad (90)$$

(cf. Eq. (21)), hence the AF in this case reduces to the expected bed-of-nails with the spacing $N_g/T_g = \nu_g$ in frequency. The effect of $\beta_g > 0$, and thus $\kappa > 0$, is two-fold: First, the shift in its first argument gives rise to the shearing of the bed-of-nails,

i.e., the frequency shift by $p\beta_g\nu_f/N_g$ of the p -th column of peaks. The second effect is the distortion of the ν -dependence of the peaks, such as observed in their second row in Figs. 9(a) and 10(a). To describe this behavior, we consider the m -th row of peaks and set $\nu = m\nu_g + \eta$, with $|\eta| \ll \nu_g$. The sum in Eq. (89) can be then approximated by the integral over the variable $s := \tau_g n$,

$$S\left(m\nu_g + \eta, \frac{\beta_g\tau_g}{2N_g}(m\nu_g + \eta)\right) \approx \nu_g \int_{-T_g/2}^{T_g/2} ds e^{2\pi i \eta s} e^{-2\pi i m B_g s^2/2T_g} \quad (91)$$

– an expression closely analogous to the Fourier transform of the conventional chirp signal. For $m = 0$, the result is simply

$$S\left(\eta, \frac{\beta_g\tau_g}{2N_g}\eta\right) \approx N_g \text{sinc}(T_g\eta), \quad (92)$$

the same as for $\beta_g = 0$. For $m \geq 1$ the integral (91) can be expressed in terms of the function

$$\mathcal{E}(x) := C(x) - iS(x), \quad (93)$$

where C and S are the Fresnel cosine and sine integrals ([10], Ch. 7.3),

$$C(x) := \int_0^x dt \cos \frac{\pi t^2}{2}, \quad S(x) := \int_0^x dt \sin \frac{\pi t^2}{2}. \quad (94)$$

The result is

$$\begin{aligned} & S\left(m\nu_g + \eta, \frac{\beta_g\tau_g}{2N_g}(m\nu_g + \eta)\right) \\ & \approx \nu_g \sqrt{\frac{T_g}{2mB_g}} e^{-i\pi T_g \eta^2/mB_g} \\ & \left[\mathcal{E}\left(\sqrt{\frac{2T_g}{mB_g}}\left(\frac{mB_g}{2} + \eta\right)\right) + \mathcal{E}\left(\sqrt{\frac{2T_g}{mB_g}}\left(\frac{mB_g}{2} - \eta\right)\right) \right] \\ & \approx \nu_g \sqrt{\frac{T_g}{2mB_g}} e^{-i\pi T_g \eta^2/mB_g} \text{rect}\left(\frac{\eta}{mB_g}\right), \end{aligned} \quad (95)$$

where the last, crude, approximation applies when $T_g B_g \gg 1$. The formulae (88), (92), and (95) imply Eq. (58) for the slope of the shear and explain the main features of the AFs represented in Figs. 9 and 10.

ACKNOWLEDGMENT

This work was supported by the Air Force Office of Scientific Research under the grant number FA9550-12-1-0121.

REFERENCES

- [1] E. Bleszynski, M. Bleszynski, T. Jaroszewicz, and R. Albanese, "Analysis of dispersive effects and enhanced medium penetrability in wide-band pulse propagation through sparse discrete media," *IEEE Transactions on Antennas and Propagation*, vol. 60, pp. 3265–3277, 2012.
- [2] E. H. Bleszynski, M. C. Bleszynski, T. Jaroszewicz, and R. Albanese, "Imaging through obscuring, discrete-scatterer media with chirped trains of wide-band pulses," *IEEE Transactions on Antennas and Propagation*, vol. 61, pp. 310–319, 2013.

- [3] J. R. Klauder, A. C. Price, S. Darlington, and W. J. Albersheim, "The theory and design of chirp radars," *Bell Syst. Tech. J.*, vol. 39, pp. 745–808, 1960.
- [4] J. B. Resnick, "High resolution waveforms suitable for a multiple target environment," Ph.D. dissertation, Massachusetts Institute of Technology, 1962.
- [5] A. W. Rihaczek, "Radar resolution properties of pulse trains," *Proceedings of the IEEE*, vol. 52, pp. 153–164, 1964.
- [6] —, "Radar waveform selection - a simplified approach," *IEEE Transactions on Aerospace and Electronic Systems*, vol. AES-7, pp. 1078–1086, 1971.
- [7] N. Levanon and E. Mozeson, *Radar signals*. Wiley-Interscience, 2004.
- [8] R. A. Albanese and R. L. Medina, "Materials identification synthetic aperture radar: progress toward a realized capability," *Inverse Problems*, vol. 29, no. 5, p. 054001 (11pp), 2013.
- [9] J. R. Partington, *Interpolation, identification, and sampling*. Oxford University Press, 1997.
- [10] M. Abramowitz and I. Stegun, *Handbook of Mathematical Functions*. Cambridge, MA: National Bureau of Standards, 1964.
- [11] R. N. Bracewell, *The Fourier transform and its applications*. New York: McGraw-Hill, 2000.
- [12] P. M. Woodward, *Probability and information theory, with applications to radar*. Pergamon Press, 1964.
- [13] L. Cohen, "Time-frequency distributions – a review," *Proceedings of the IEEE*, vol. 77, pp. 941–981, 1989.
- [14] D. C. Munson Jr., J. D. O'Brien, and W. K. Jenkins, "A tomographic formulation of spotlight mode synthetic aperture radar," *Proc. IEEE*, vol. 72, pp. 917–925, 1983.
- [15] M. D. Desai and W. K. Jenkins, "Convolution backprojection image reconstruction for spotlight mode synthetic aperture radar," *IEEE Transactions on Image Processing*, vol. 1, pp. 505–517, 1992.
- [16] M. Cheney, "A mathematical tutorial on synthetic aperture radar," *SIAM Review*, vol. 43, pp. 301–312, 2001.
- [17] E. Chuang, S. Hensley, and K. Wheeler, "A highly capable arbitrary waveform generator for next generation radar systems," in *2006 IEEE Aerospace Conference*. IEEE, 2006, pp. 7–pp.
- [18] T. Alpert, M. Werz, F. Lang, D. Ferenci, M. Masini, M. Groezing, and M. Berroth, "Arbitrary waveform generator based on FPGA and high-speed DAC with real-time interface," in *2012 8th Conference on Ph. D. Research in Microelectronics and Electronics (PRIME)*, 2012, pp. 1–4.
- [19] I. S. Gradshteyn and I. M. Ryzhik, *Tables of Integrals, Series, and Products*, 7th ed. Academic Press, 2007.
- [20] E. Bedrosian, "The analytic signal representation of modulated waveforms," *Proceedings of the IRE*, vol. 50, no. 10, pp. 2071–2076, 1962.

Appendix B

Doppler effects in time-resolved intensity of optical pulses propagating through moving particulate atmospheric media

Abstract

Propagation of optical and infrared pulses through moving atmospheric particulate media is investigated. The radiative transfer equation (RTE) is generalized to describe effects of the Doppler frequency shift on the time-resolved specific intensity of pulses. The overall effect of the frequency shift is estimated and found to be small, as a result of cancellation of phase variations in the the pulse intensity. That cancellation is nearly perfect in the pulse component associated with “early-time diffusion”, i.e., in the early-time steeply rising structure due to small-angle diffractive scattering on medium constituents.

1 Radiative transfer equation with moving scatterers

We provide here a short summary of how propagation of the mutual coherence function (MCF) of electromagnetic pulses propagating in a time-dependent particulate random medium can be described by means of the the radiative transfer equation (RTE).

Assumptions about the medium and the propagating pulse. We consider here an infinite, statistically homogeneous and isotropic medium. The medium is assumed to be dilute, i.e., the average scatterer-scatterer distance d_0 large compared to the carrier wavelength,

$$d_0 \gg \lambda_0 \equiv \frac{c}{\nu_0} \quad (1)$$

($\nu_0 = \omega_0/(2\pi)$ is the carrier frequency), while the scatterer radius a may be comparable with the carrier wavelength. The above assumptions ensure a large mean free path $\ell_t = 1/(n_0 \sigma_t(\omega_0))$, defined in terms of the scatterer number density $n_0 = 1/d_0^3$ and the total cross-section on a single scatterer (associated with coherent wave propagation). Since, assuming non-resonant scattering, the cross-section is approximately bounded by its geometrical scattering value, $\sigma_t(\omega_0) \lesssim 2\pi a^2$, we also have

$$\ell_t \gtrsim \frac{d_0^3}{2\pi a^2} \gg d_0 \gg \lambda_0 . \quad (2)$$

The pulse is assumed to be narrow-banded, in the sense of bandwidth B small compared to the carrier frequency ν_0 . When considering early time diffusion we will additionally

assume that the pulse duration $T_p = 1/B$ is sufficiently small, such that its physical extent $cT_p = c/B$ is smaller than the mean free path. These two conditions are equivalent to

$$\frac{c}{\ell_t} < B \ll \nu_0 . \quad (3)$$

These above assumptions hold in propagation of typical short optical and infrared pulses through atmospheric obscuring media, such as clouds or fog. For $\lambda_0 \sim 1 \mu\text{m}$, $d_0 \sim 1\text{mm}$, and $a \lesssim 5 \mu\text{m}$ the mean free path is of the order $\ell_t \gtrsim 10\text{m}$. Even a short pulse of duration $T = 1/B \sim 1\text{ps}$ satisfies the second condition in Eq. (3), i.e., $B \sim 1\text{THz} \ll \nu_0 \sim 300\text{THz}$. The first condition holds for pulses of duration less than $\ell_t/c \sim 30\text{ns}$.

Formulating transport equations even for *static* statistically *inhomogeneous* media is a difficult problem, still subject to some controversy. Therefore, since our main objective is to assess the effects of medium motion, we will concentrate on situations where the medium can be considered statistically uniform, at least over domains (“samples”) of sizes L larger than or comparable to the mean free path ℓ_t , i.e., on the scale of distances between two consecutive interactions (as understood in the context of transport equations).

The above assumption, together with the previously assumed properties of the propagating pulse, allows to treat the considered medium sample as statistically homogeneous and uniformly moving with a constant velocity. Since we are concerned with terrestrial atmospheric media (rather than possible astrophysical applications involving relativistic gases, plasmas, etc.) the medium motion velocities V are typical of winds and certainly below the speed of sound, $V < 340\text{m/s}$. Therefore, the magnitude of the first-order Doppler effects is at most

$$\frac{V}{c} < 1.2 \cdot 10^{-6} ; \quad (4)$$

the fact that such effects may not be negligible, is due to other factors appearing in observable quantities, e.g., a large number of signal periods during the measurement time, a large number of wavelength in the interferometer cavity, etc.

The radiative transfer equation (RTE). The main physical quantity we will be concerned with, will be the mutual coherence function, i.e., the ensemble-averaged Green function of the product of a field and its complex conjugate,¹

$$\Gamma(t; \tau, \tau'; \mathbf{R}; \mathbf{r}, \mathbf{r}') := 4\pi \langle u_{\tau'/2, \mathbf{r}'/2}(t + \tau/2; \mathbf{R} + \mathbf{r}/2) u_{-\tau'/2, -\mathbf{r}'/2}^*(t - \tau/2; \mathbf{R} - \mathbf{r}/2) \rangle , \quad (5)$$

where $u_{t, \mathbf{r}}$ is a field emitted by an instantaneous point source at the time t and location \mathbf{r} . Because of the assumed linearity of the medium response, the mutual coherence function (MCF) of fields generated by any source can be obtained by calculating a convolution of the Green function (5) with the source distribution.

Starting with the above MCF, one can obtain, under the assumptions specified above, a modified radiative transfer equation (RTE) taking into account motion of the particulate medium. The derivation proceeds through the usual steps of obtaining an approximate forms of the Dyson equation (DE) for the ensemble average of the coherent propagating

¹ The factor 4π in the definition (5) has been introduced in order to normalize the MCF in the same way as the energy flux.

field and then of the Bethe-Salpeter equation for the MCF; under the assumption of high frequencies and a dilute medium, the latter equation is reduced to RTE. In these steps, however, we take into account effects of the medium motion: after expressing the kernels of the DE and the RTE in terms of the amplitudes and cross-sections for scattering on a single medium constituent, we modify these amplitudes (in a rigorous way) by including the motion of the scatterer.

The final result for a statistically homogeneous medium domain, uniformly moving with a velocity \mathbf{V} is the Fourier-space “generalized RTE” for the Green function $\tilde{\Gamma}_{\mathbf{V}}(\omega_0; \Omega, \omega; \mathbf{P}, \hat{\mathbf{s}}, \hat{\mathbf{s}}')$, where $\hat{\mathbf{s}}$ and $\hat{\mathbf{s}}'$ are the final and initial energy flux propagation directions, and the meaning of the frequency Ω and the wave number \mathbf{P} is explained by its relation to the MCF (5),

$$\Gamma_{\mathbf{V}}(t; \tau, \tau'; \mathbf{R}; \mathbf{r}, \mathbf{r}') = \int \frac{d\Omega}{2\pi} \frac{d\omega}{2\pi} \frac{d\omega_0}{2\pi} \frac{d^3P}{(2\pi)^3} \int \frac{d^2\hat{s}}{4\pi} \frac{d^2\hat{s}'}{4\pi} \quad (6)$$

$$e^{-i\Omega t} e^{-i\omega\tau} e^{i\omega_0\tau'} e^{i\mathbf{P}\cdot\mathbf{R}} e^{-ik(\omega)\hat{\mathbf{s}}\cdot\mathbf{r}} e^{ik(\omega_0)\hat{\mathbf{s}}_0\cdot\mathbf{r}'} \tilde{\Gamma}_{\mathbf{V}}(\omega_0, \Omega, \omega; \mathbf{P}, \hat{\mathbf{s}}, \hat{\mathbf{s}}_0) ,$$

where $k(\omega) \equiv \omega/v_0$ and $v_0 \approx c$ is the propagation speed of the coherent wave in the effective medium (discussed below). Hence, the wave number \mathbf{P} is associated through the Fourier transform with the mid-point propagation distance \mathbf{R} ; the frequency variable Ω is Fourier-conjugate to the mid-point time variable t and the variables ω and ω_0 are conjugate to the observation and source relative time variables τ and τ' ; finally, the relative coordinates \mathbf{r} and \mathbf{r}' are associated with the energy flux directions $\hat{\mathbf{s}}$ and $\hat{\mathbf{s}}_0$.

The obtained RTE has the form

$$\begin{aligned} \tilde{\Gamma}_{\mathbf{V}}(\omega_0; \Omega, \omega; \mathbf{P}, \hat{\mathbf{s}}, \hat{\mathbf{s}}') - \tilde{G}_{\mathbf{V}}(\Omega, \omega; \mathbf{P}, \hat{\mathbf{s}}) \int d^2\hat{s}'' \tilde{\Sigma}_s(\omega, \omega - \omega/v_0 \mathbf{V} \cdot (\hat{\mathbf{s}} - \hat{\mathbf{s}}''); \hat{\mathbf{s}}, \hat{\mathbf{s}}'') \\ \tilde{\Gamma}_{\mathbf{V}}(\omega_0; \Omega, \omega - \omega/v_0 \mathbf{V} \cdot (\hat{\mathbf{s}} - \hat{\mathbf{s}}''); \mathbf{P}, \hat{\mathbf{s}}'', \hat{\mathbf{s}}') \quad (7) \\ = 2\pi \delta(\omega - \omega_0) \delta^2(\hat{\mathbf{s}} - \hat{\mathbf{s}}') \tilde{G}_{\mathbf{V}}(\Omega, \omega; \mathbf{P}, \hat{\mathbf{s}}) \end{aligned}$$

with the “RTE two-field Green function”

$$\tilde{G}_{\mathbf{V}}(\Omega, \omega; \mathbf{P}, \hat{\mathbf{s}}) := \frac{1}{\mu_t(\omega - \omega/v_0 \mathbf{V} \cdot \hat{\mathbf{s}}) - i(\Omega/v_0 - \mathbf{P} \cdot \hat{\mathbf{s}})} \quad (8)$$

describing coherent-wave propagation in the effective medium, and involving the attenuation coefficient

$$\mu_t(\omega) = n_0 \sigma_t(\omega) ;$$

finally, the “scattering function”

$$\tilde{\Sigma}_s(\omega, \omega'; \hat{\mathbf{s}}, \hat{\mathbf{s}}') = n_0 \sigma_s(\omega, \omega'; \hat{\mathbf{s}}, \hat{\mathbf{s}}') ;$$

is expressed in terms of the differential scattering cross-section σ_s , in which $\hat{\mathbf{s}}$ and $\hat{\mathbf{s}}'$ are the directions of the final and initial wave vectors, and ω and ω' are the corresponding Doppler-shifted frequencies, as illustrated in Fig. 1.

The RTE (7) is similar to that obtained by Ishimaru, except that the latter does not take into account frequency shifts in coherent scattering.

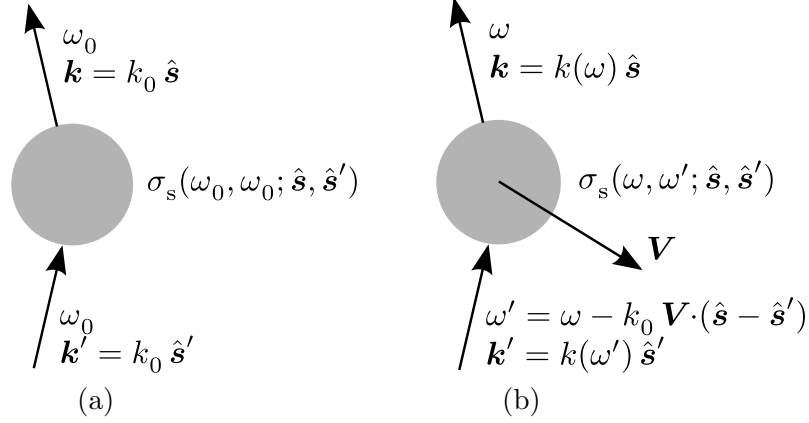


Figure 1: (a) Scattering on a single stationary particle, with a fixed frequency ω_0 and $k_0 = k(\omega_0)$; in general, $k(\omega) \equiv \omega/v_0$. (b) Scattering on a moving particle with a frequency change.

Some notable features of the generalized RTE (7) are as follows:

- The kernel depends in a nontrivial way on ω , i.e., different ω values are coupled in the equation.
- The solution also depends on ω : if the source emits a signal with a fixed $\omega = \omega_0$, the solution will contain a continuum of ω values centered about ω_0 .
- According to Eq. (6), the spread of the solution in ω affects the MCF dependence on the relative time τ . In particular, the Green function evaluated at $\tau = 0$ and $\mathbf{r} = \mathbf{0}$ (the analogue of the ordinary specific intensity), involves only the ω -integral of the solution (7),

$$\Gamma_{\mathbf{V}}(t; 0, \tau'; \mathbf{R}; \mathbf{0}, \mathbf{r}') = \int \frac{d\Omega}{2\pi} \frac{d\omega_0}{2\pi} \frac{d^3P}{(2\pi)^3} \int \frac{d^2\hat{s}}{4\pi} e^{-i\Omega t} e^{i\omega_0 \tau'} e^{i\mathbf{P} \cdot \mathbf{R}} e^{ik(\omega_0) \hat{\mathbf{s}}_0 \cdot \mathbf{r}'} \hat{\Gamma}_{\mathbf{V}}(\omega_0, \Omega; \mathbf{P}, \hat{\mathbf{s}}_0), \quad (9)$$

with

$$\hat{\Gamma}_{\mathbf{V}}(\omega_0, \Omega; \mathbf{P}, \hat{\mathbf{s}}_0) = \int \frac{d\omega}{2\pi} \int \frac{d^2\hat{s}}{4\pi} \tilde{\Gamma}_{\mathbf{V}}(\omega_0, \Omega, \omega; \mathbf{P}, \hat{\mathbf{s}}, \hat{\mathbf{s}}_0). \quad (10)$$

Small variations in the cross-section. Suppose now the frequency dependence of the scattering cross-section is sufficiently weak, so that the scattering function $\Sigma_{\mathbf{V}}$ and the Green function $G_{\mathbf{V}}$ in the RTE (7) can be evaluated at the carrier frequency, i.e., one can approximate

$$\tilde{\Sigma}_{\mathbf{s}}(\omega, \omega - k_0 \mathbf{V} \cdot (\hat{\mathbf{s}} - \hat{\mathbf{s}}''); \hat{\mathbf{s}}, \hat{\mathbf{s}}') \rightsquigarrow \tilde{\Sigma}_{\mathbf{s}}(\omega_0; \hat{\mathbf{s}}, \hat{\mathbf{s}}') := n_0 \sigma_{\mathbf{s}}(\omega_0, \omega_0; \hat{\mathbf{s}}, \hat{\mathbf{s}}') \quad (11a)$$

and

$$\tilde{G}_{\mathbf{V}}(\Omega, \omega; \mathbf{P}, \hat{\mathbf{s}}) \rightsquigarrow \tilde{G}(\Omega, \omega_0; \mathbf{P}, \hat{\mathbf{s}}) := \frac{1}{\mu_t(\omega_0) - i(\Omega/v_0 - \mathbf{P} \cdot \hat{\mathbf{s}})} \quad (11b)$$

with

$$\mu_t(\omega_0) = n_0 \sigma_t(\omega_0) . \quad (11c)$$

In this limit the Green and the scattering functions in the RTE become independent of the medium motion and the function $\hat{F}_{\mathbf{V}}(\omega_0; \Omega, \omega_0; \mathbf{P}, \hat{\mathbf{s}}, \hat{\mathbf{s}}') \equiv \hat{F}(\Omega, \omega_0; \mathbf{P}, \hat{\mathbf{s}}, \hat{\mathbf{s}}')$ satisfies the ordinary RTE

$$\begin{aligned} \hat{F}(\Omega, \omega_0; \mathbf{P}, \hat{\mathbf{s}}, \hat{\mathbf{s}}') - \tilde{G}(\Omega, \omega_0; \mathbf{P}; \hat{\mathbf{s}}) \int d^2 \hat{\mathbf{s}}'' \tilde{\Sigma}_s(\omega_0; \hat{\mathbf{s}} \cdot \hat{\mathbf{s}}'') \hat{F}(\Omega, \omega_0; \mathbf{P}, \hat{\mathbf{s}}'', \hat{\mathbf{s}}') \\ = \delta^2(\hat{\mathbf{s}} - \hat{\mathbf{s}}') \tilde{G}(\Omega, \omega_0; \mathbf{P}, \hat{\mathbf{s}}) . \end{aligned}$$

2 Estimates of the Doppler shift effects in the RTE

The analysis conducted above indicates that the medium motion affects the intensity only if there is a *significant dispersion* in scattering on the individual medium constituents.

However, implementation of the ω -dependent RTE (as an integral equation) would be substantially more involved than for the ordinary RTE. In particular,

- for a statistically homogeneous infinite medium the solution of the ordinary RTE can be expanded in spherical harmonics in the angles of $\hat{\mathbf{s}}$ relative to $\hat{\mathbf{P}}$,
- the ω -dependent RTE solution is a function of both $\hat{\mathbf{P}} \cdot \hat{\mathbf{s}}$ and $\hat{\mathbf{V}} \cdot \hat{\mathbf{s}}$ and the partial-wave expansion becomes considerably more complicated,
- for a statistically homogeneous infinite medium the ordinary RTE reduces to an algebraic (matrix) equation,
- the ω -dependent RTE would not reduce to an algebraic equation, but would remain a Fredholm integral equation (of the second kind).

At the same time, implementation of the ω -dependent RTE as a Monte Carlo solution would be also rather complex and computationally intensive: it would require introducing the relative time as an additional degree of freedom and making interactions with the scatterers nonlocal in that time (we stress again that the Doppler shift is *not* directly related to the time delay and to the pulse length)

Therefore, we concentrate first on the following question: how much dispersion is there within the the Doppler shift range?

- The upper bound on the frequency shift is

$$|\Delta \omega_D| \leq \frac{2v}{c} \omega_0 .$$

We take, as an estimate, the droplet speed $v = 340 \text{ m/s}$ (the speed of sound) and assume the carrier wavelength $\lambda_0 = 0.633 \mu\text{m}$ (the red-light HeNe laser). Then the carrier frequency and its spread are

$$\begin{aligned} \nu_0 &= \frac{\omega_0}{2\pi} \approx 474 \text{ THz} = 4.74 \cdot 10^{14} \text{ Hz} , \\ \Delta \nu_D &= \frac{\Delta \omega_D}{2\pi} \approx 2.1 \text{ GHz} = 2.1 \cdot 10^9 \text{ Hz} , \end{aligned}$$

and the corresponding relative spread in the wavelength is

$$\frac{|\Delta \lambda_D|}{\lambda_0} \leq \frac{2v}{c} \approx 2.3 \cdot 10^{-6}.$$

Hence, the considered Doppler induced wavelength range is

$$\lambda = (0.633 \pm 1.4 \cdot 10^{-6}) \mu\text{m}$$

or

$$\begin{aligned} \lambda_{\max} &= 0.6330014 \mu\text{m}, \\ \lambda_0 &= 0.6330000 \mu\text{m}, \\ \lambda_{\min} &= 0.6329986 \mu\text{m}. \end{aligned}$$

We note that the above bounds correspond to $|\hat{\mathbf{s}} - \hat{\mathbf{s}}'| = 2$, i.e., to the backward scattering situation. Early-time diffusion is mostly due to much smaller angles, $\theta \lesssim 6^\circ$, hence $|\hat{\mathbf{s}} - \hat{\mathbf{s}}'| \lesssim 0.1$, hence the expected frequency shifts will be about 20 times smaller. Also, in realistic situations, the droplet speeds are not likely to be as high as the ones used in the above estimates.

The typical duration, bandwidth, and the wavelength spread of the “early-time diffusion” pulses are

$$\begin{aligned} \Delta t_p &= 100 \text{ ps}, \\ \Delta \nu_p &= \frac{1}{\Delta t_p} \approx 10 \text{ GHz}, \\ \frac{|\Delta \lambda_p|}{\lambda_0} &= \frac{\Delta \nu_p}{\nu_0} \approx 2.1 \cdot 10^{-5}. \end{aligned}$$

The resulting Doppler shift $\Delta \nu_D \approx 2.1 \text{ GHz}$ is relatively small, but not negligible, in comparison with the typical duration and bandwidth of the early-time diffusion pulses.

- We will now proceed to assess variations of the integrated and differential scattering cross-sections which might result from the motion-induced frequency variations in the RTE and their impact on the early -time diffusion component of the signal.

In the example given below, we assume

- the medium to be an ensemble of gamma-distributed water droplets with the shape parameter $\nu = 10$ and the r.m.s. radius $\bar{a} = 5 \mu\text{m}$
- the band of Doppler induced frequencies (wavelengths)

$$\begin{aligned} \lambda_{\max} &= 0.633005 \mu\text{m}, \\ \lambda_0 &= 0.633000 \mu\text{m}, \\ \lambda_{\min} &= 0.632993 \mu\text{m}. \end{aligned}$$

It is known that scattering on a water droplet is dispersive, i.e., its cross-section can change rapidly with the frequency. However, Fig. 2 shows that although the Mie resonances are indeed observed and the cross-section changes significantly,

- the relative spacing between the Mie resonances,

$$\frac{|\Delta \lambda_M|}{\lambda_0} \gtrsim 0.006$$

is still much larger than the Doppler shift of interest

$$\frac{|\Delta \lambda_D|}{\lambda_0} \leq \frac{2v}{c} \approx 2.3 \cdot 10^{-6}.$$

Fig. 3 shows differential cross sections for the carrier and two (up- and down-) Doppler shift frequencies (wavelengths). We observe that the differential cross-section change negligibly over the Doppler shift band.

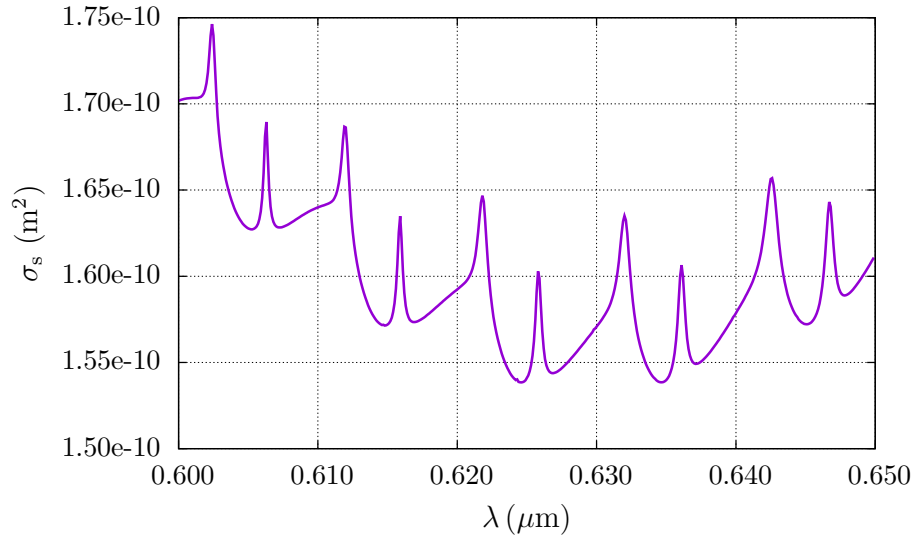


Figure 2: Wavelength dependence of the integrated scattering cross-section for a water droplet of radius $a = 5 \mu\text{m}$.

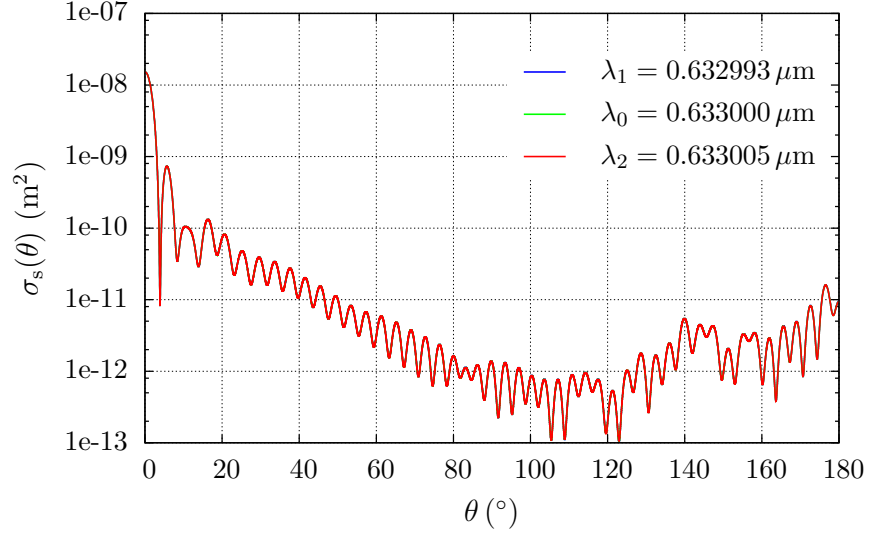


Figure 3: Differential cross-sections for the three wavelengths (the carrier wavelength and the wavelengths corresponding to the up- and down- Doppler shifts). The water droplet radius is $a = 5 \mu\text{m}$.

Figs. 2 and 3 indicate that (for reasonable assumptions about the droplet size distribution) the value of the droplet cross-section can be, within a good approximation, assumed constant within the frequency range cause by the Doppler shift.

Fig. 4 shows the time resolved specific intensity for two wavelengths corresponding to the up- and down- Doppler shifts. The results indicate that the early-time intensity can be potentially very weakly sensitive to the medium motion.

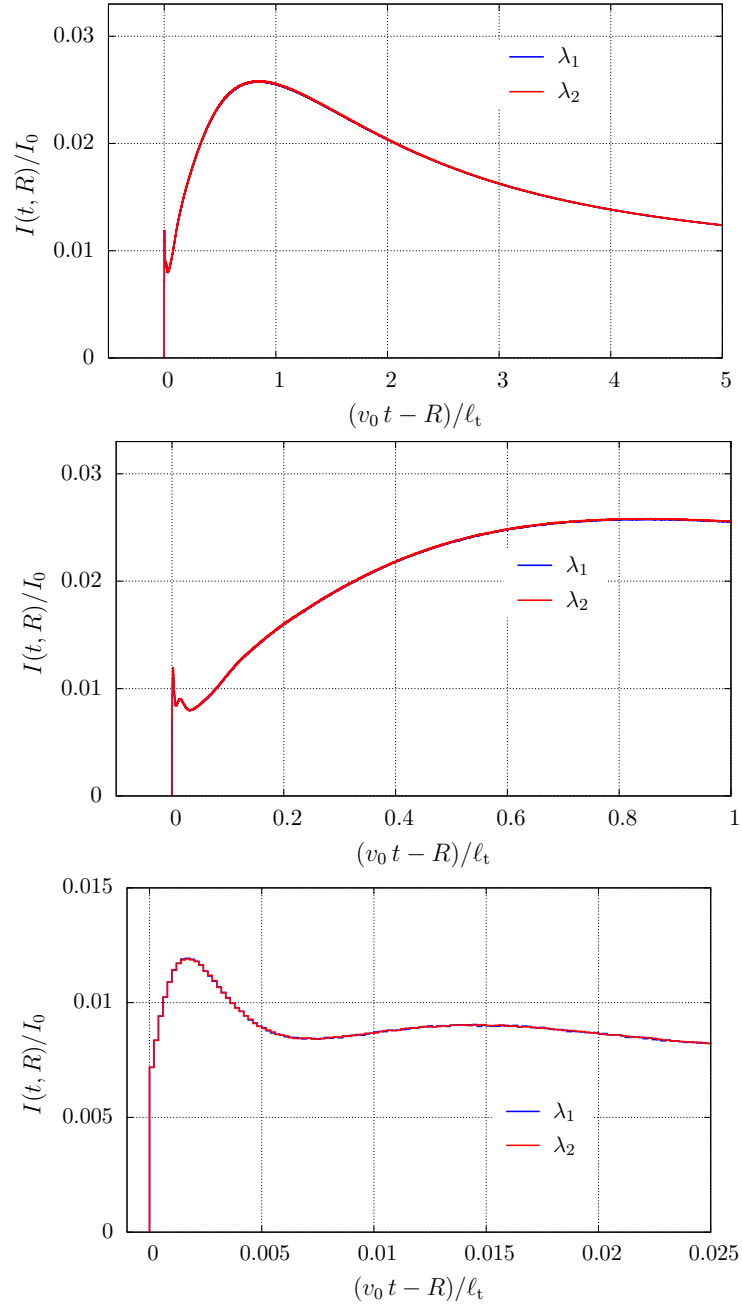


Figure 4: Time-resolved intensities for the two wavelengths corresponding to the up- and down- Doppler shifts. The middle and bottom plots are the same as the top plot but the early-time interval is extended.

1.

1. Report Type

Final Report

Primary Contact E-mail**Contact email if there is a problem with the report.**

elizabeth@monopoleresearch.com

Primary Contact Phone Number**Contact phone number if there is a problem with the report**

805-375-0317

Organization / Institution name

Monopole Research

Grant/Contract Title**The full title of the funded effort.**

Imaging through random discrete-scatterer dispersive media

Grant/Contract Number**AFOSR assigned control number. It must begin with "FA9550" or "F49620" or "FA2386".**

FA9550-12-1-0121

Principal Investigator Name**The full name of the principal investigator on the grant or contract.**

Elizabeth H. Bleszynski

Program Manager**The AFOSR Program Manager currently assigned to the award**

Arje Nachman

Reporting Period Start Date

04/15/2012

Reporting Period End Date

08/14/2015

Abstract

The objective of the effort was to develop a methodology which would allow enhanced signal transmission, high resolution range imaging and/or target detection through optically obscuring, dilute, discrete-scatterer media such as atmospheric clouds, fog, dust and other aerosols.

(A) Properties of chirped-train waveforms such as their multi-band power spectra and the resulting point spread and ambiguity functions were analyzed. Advantages of the utilization of chirped trains in "multi-spectral" imaging (i.e., imaging based on frequency sub-bands of the chirped train signal) allowing extraction of frequency dependent information with improved signal-to-noise ratio were observed.

(B) Propagation of short infrared/optical pulses in dilute random media consisting of large, compared to the wavelength, scatterers was analyzed. A rigorous approach based on analytic complex-contour integration of numerically determined cut and pole singularities of the radiative transport equation solution in the Fourier space was developed. It was found that the intensity of a propagating pulse, in addition to the coherent ("ballistic") contribution and a long late-time diffusive tail, also exhibits a sharply rising early-time component that (i) can be attributed to the small-angle diffractive part of the scattering cross-section on medium particles, (ii) is attenuated proportionally to the nondiffractive rather than the total cross-section, (iii) can be extracted by high-pass filtering of the received pulse without invoking time gating procedures and, (iv) is very weakly sensitive to the medium motion.

DISTRIBUTION A: Distribution approved for public release.

Distribution Statement

This is block 12 on the SF298 form.

Distribution A - Approved for Public Release

Explanation for Distribution Statement

If this is not approved for public release, please provide a short explanation. E.g., contains proprietary information.

SF298 Form

Please attach your [SF298](#) form. A blank SF298 can be found [here](#). Please do not password protect or secure the PDF. The maximum file size for an SF298 is 50MB.

[sf298_FA9550-12-1-0121.pdf](#)

Upload the Report Document. File must be a PDF. Please do not password protect or secure the PDF . The maximum file size for the Report Document is 50MB.

[final_report_FA9550-12-1-0121.pdf](#)

Upload a Report Document, if any. The maximum file size for the Report Document is 50MB.

Archival Publications (published) during reporting period:

Changes in research objectives (if any):

Change in AFOSR Program Manager, if any:

Extensions granted or milestones slipped, if any:

AFOSR LRIR Number

LRIR Title

Reporting Period

Laboratory Task Manager

Program Officer

Research Objectives

Technical Summary

Funding Summary by Cost Category (by FY, \$K)

	Starting FY	FY+1	FY+2
Salary			
Equipment/Facilities			
Supplies			
Total			

Report Document

Report Document - Text Analysis

Report Document - Text Analysis

Appendix Documents

2. Thank You

E-mail user

Aug 20, 2015 20:50:56 Success: Email Sent to: elizabeth@monopoleresearch.com